Acoustic Monitoring of DC Plasma Arcs

by

John James Burchell

Thesis submitted in fulfilment
of the requirements for the Degree
of

MASTER OF SCIENCE IN ENGINEERING
(EXTRACTIVE METALLURGY)

in the Department of Process Engineering
at the University of Stellenbosch

Supervised by

Prof. J.J. Eksteen
Dr T. Niesler
Prof. C. Aldrich

STELLENBOSCH

March 2008

Declaration

I, the undersigned, hereby declare that the work contained in this thesis is my own and has not previously been submitted in partial or entirety for any degree or examination.

John James Burchell

November 29, 2007

Abstract

The arc, generated between the cathode and slag in a dc electric arc furnace (EAF), constitutes the principal source of thermal energy in the furnace. Steady state melting conditions rely on efficient control of the arc's power. This is achieved by keeping the arc's length constant, which is currently not directly measured in the industry, but relies on an external voltage measurement. This voltage measurement is often subject to inaccuracies since it may be influenced by voltage fluctuations that are not necessarily related to the arc itself, such as the variable impedance of the molten bath and the degradation of the graphite electrode. This study investigated whether or not it is possible to develop a sensor for the detection of arc length from the sound that is generated by the arc during operation.

Acoustic signals were recorded at different arc lengths using a 60 kW dc electric arc furnace and 600 g of mild steel as melt. Using a filterbank kernel (FB) based Fisher discriminant analysis (KFD) method, nonlinear features were extracted from these signals. The features were then used to train and test a k nearest neighbour (kNN) classifier.

Two methods were used to evaluate the performance of the kNN classifier. In the first, both test and train features were extracted from acoustic signals recorded during the same experimental run and used a ten fold bootstrap method for integrity. The second method tested the generalized performance of the classifier. This involved training the kNN classifier with features extracted from the acoustic recordings made during a single or multiple experimental runs and then testing it with features drawn from the remaining experimental runs.

The results from this study shows that there exists a relationship between arc length and arc acoustic which can be exploited to develop a sensor for the

detection of arc length from arc acoustics in the dc EAF. Indications are that the performance of such a sensor would rely strongly on how statistically representative the acoustic data are, used to develop the sensor, to the acoustics generated by industrial dc EAFs during operation.

Oorsig

Die boog tussen die katode en slak in 'n gelykstroom boogoond, is die hoofbron van termiese energie in die oond. Bestendige smelttoestande in die oond hang sterk af van die effektiewe beheer van die lengte van die boog wat tans nie direk gemeet word nie. Die booglengte is op die oomblik afhanklik van 'n eksterne spanningsmeting en is dus dikwels onakkuraat deurdat die meting beïnvloed word deur wisselende spanningsvlakke wat nie noodwendig iets te doen het met 'n verandering in booglengte nie (soos die wisselvaligheid van die bad se impedansie en die konstante verwering van die katode tydens oondwerking). Die studie het die lewensvatbaarheid van 'n meetinstrument ondersoek wat die booglengte bepaal het vanaf die akoestiek van die boog in 'n gelykstroom boogoond.

Akoestiese seine is opgeneem by verskillende booglengtes deur gebruik te maak van 'n 60 kW gelykstroom boogoond met 600 g weekstaal as gesmelte lading. 'n Filterbank (FB) - kerngebaseerde Fisher diskriminant analise (KFD) is gebruik om eienskappe of komponente uit die akoestiese seine uit te haal. Hierdie komponente is toe gebruik om 'n k naaste buurman (kNN) klassifiseerder mee te leer.

Twee metodes is gebruik om die prestasie van die kNN klassifiseerder te ontleed. In die eerste metode is die komponente waarmee die klassifiseerder geleer en getoets is uit 'n enkele eksperiment se data geneem. In die tweede metode was die leerkomponente uit verskillende eksperimente geneem as die toetskomponente om sodoende die algemene prestasie van die klassifiseerder te toets.

Die resultate van die studie toon dat daar 'n verhouding bestaan tussen die lengte van 'n boog en die klank wat die boog opwek, asook dat 'n meetinstrument ontwikkel kan word wat die verhouding kan gebruik om die lengte van die boog te meet. Die studie dui aan dat die prestasie van so 'n

meetinstument sterk sal afhang van hoe statisties verteenwoordigend die data is waarmee die meetinstrument geleer sal word t.o.v. die data wat dit sal teekom in die industrie.

Table of Contents

Chapter 1

Introduction

The demand for ferroalloy and deoxidizing agents in steel led to the development of the first industrial scale arc furnaces at the beginning of the twentieth century (Kunze et al., 2004). From an industrial perspective, these furnaces were required to operate from the local power grid and hence they were alternating current (ac) electric arc furnaces (EAFs). It was not until the advent of semiconductor technology, and hence the rectifier, in the early 1970's that the direct current (dc) EAF became an industrially viable option.

The dc EAF is currently employed in the South African context at Samancor for the remelting of ferrochrome fines and at Namakwa Sands for the production of T_iO_2 and pig iron. Both processes use technology developed by the South African mineral technology science council (Mintek). Mintek has also pioneered the utilization of a dc EAF in the process of recovering cobalt from waste slag, used at the 20 Mt reverberatory furnace slag dump at Nkana, Zambia.

These applications are subject to constraints that rule out the use of the conventional submerged arc EAF (ac). It is the dc EAF's ability to process small fines (< 6mm in diameter) directly without prior agglomeration, its mutually independent electrical and metallurgical parameters, as well as its increased power efficiency and lower electrode consumption, that have resulted in its increasing popularity since its introduction in the late 1970's (Knight et al., 1990).

In the dc EAF, efficient control of the electrical power that supplies the furnace, translates to efficient thermal energy control and hence improved control of the smelting or melting operation. For this type of furnace, the voltage applied across and the current running through the arc constitute the active power delivered to the furnace. The current drawn by the dc EAF is controlled directly at the power source and the voltage is controlled by adjusting the length of the arc. Efficient arc length control is therefore integral to the operational efficiency and hence profitability of the dc EAF in any application.

The motivation for this project arose from the fact that current methods of arc length control rely on voltage measurements made externally to the furnace. These measurements are often subject to inaccuracies since they are influenced by voltage fluctuations that are not necessarily related to the arc itself, such as the variable impedance of the molten bath and the degradation of the graphite electrode. Also, since the measurement equipment that records the voltage is connected electrically to the furnace, errors are usually induced by the large current fluctuations present.

The dc EAF is affected strongly by inaccuracies in arc length control, in comparison with the submerged arc EAF which utilizes slag resistivity to perform a degree of power control. It is therefore of interest to search for alternative methods with which to control the arc length in the dc EAF. This project investigates whether or not a relationship exists between the length of the arc in a dc EAF and the sound that is generated by the arc. Such a relationship could be used to develop an acoustic sensor which is electrically isolated from the dc EAF and would therefore be insensitive to the fluctuations that are currently problematic.

This investigation presents a study in machine learning, or more specifically pattern recognition. An analysis is performed that investigate whether or not it is possible to train a computer model to recognize patterns in the acoustic

signals generated by similar arc lengths, i.e. *using this model to infer the arc length of a direct current electric arc furnace from a given acoustic signal.* The pattern recognition methodology used is discussed in Chapter 4, where signals recorded at various arc lengths are used to train predictive models. All experimentation was performed using a laboratory scale dc EAF and is discussed in Chapter 3. The results of this project are presented in Chapter 5 and a review of the literature found relevant to the project is presented in Chapter 2.

Chapter 2

Literature Review

2.1 Introduction

In this chapter the literature found relevant to the thesis is presented. Very little work has been found relating specifically to the acoustic monitoring or even the general acoustic characteristics of dc plasma arcs. However, some interesting work has been done that investigates plasma as a possible sound source or loudspeaker by Babcock et al (1968). This work, as well as that done by Drouet and Nadau, which explores the relationship between the power in alternating current (ac) arcs and the acoustic signals they generate, is reviewed in Section 2.3.

It is also important for the reader to familiarize themselves with the environment of direct current (dc) electric arc furnaces (EAFs). Section 2.2 is dedicated to providing a background of the dc EAF. More specifically Section 2.2 considers the dc EAF and its components, the plasma in the dc EAF, how other electric furnaces compare with the dc EAF, applications of the dc EAF in the South African context and finally the power source that drives it.

2.2 The dc electric arc furnace

At the beginning of the twentieth century an increase in the demand for ferroalloy and deoxidizing agents in steel lead to the development of the first industrial scale arc furnaces. The theory behind dc furnaces has existed for nearly as long as that describing ac furnaces; dc melting furnaces similar to those in use today were described as long ago as 1881 in Germany and 1885

in Sweden (Edström et al., 1987). These early dc furnaces utilized dc generators and batteries and were soon replaced by the more practical alternating current (ac) arc furnaces that could be supplied by the existing power grid. It was not until the advent of semiconductor technology in the early 1970's, and the rectifier, that dc furnaces became a practical alternative to the conventional three phase ac furnaces that had been the industry standard up to then. Figure 2.1 presents a layout of the dc EAF and its major components.

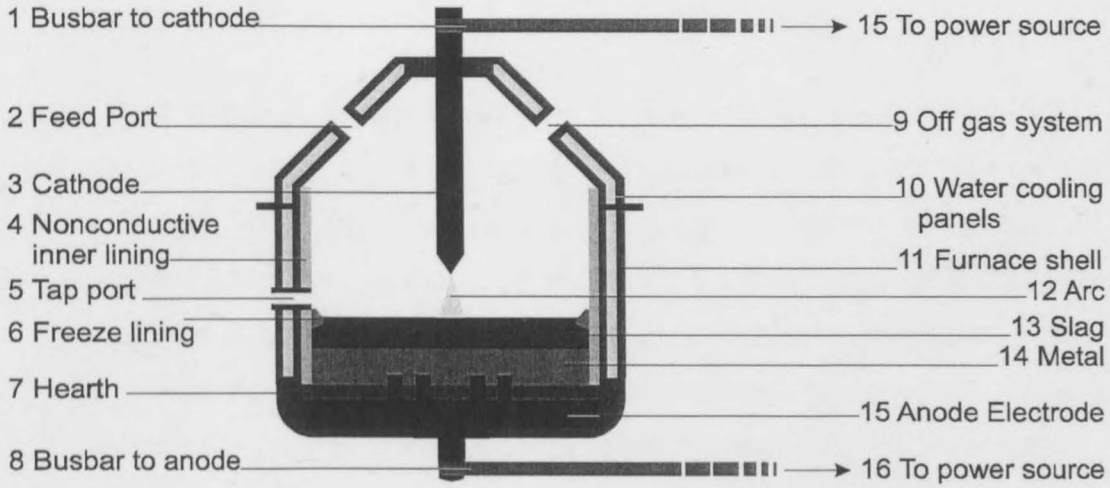

Figure 2.1. The direct current (dc) electric arc furnace (EAF) and its main components.

The dc EAF is characterized by a single graphite cathode that uses a transferred arc to perform smelting and/or melting operations. In the transferred arc arrangement the arc is struck between the cathode (negative polarity) and the melt that forms the path to the bottom anode (positive polarity). This arrangement of polarity allows the arc power to be directed towards the melt as well as to cut down on electrode consumption (Evers et al., 1999).

The following list provides a description of some of the components of the dc EAF, listed in Figure 2.1 above:

- The Freeze lining (6 in Figure 2.1) is a natural region of frozen slag and metal that forms a protective layer which separates the furnace shell (11) from the open bath (13 and 14) (Maske et al., 1985).

- The furnace shell (11) is the body of the furnace that is insulated so as to separate it electrically from the bottom anode which is at a small positive potential. The furnace shell is earthed and therefore also the melt, since connections between the melt and shell always exist due to penetrations or bridges at the tapping port (Eddström, 1987), which is the opening that allows for tapping of metal and slag from the furnace (5).

- The furnace outer shell, roof and off gas port (9) is water cooled (10) whilst the hearth (7), and inner shell is provided with insulation from a refractory lining (4). The water cooling system has to be maintained efficiently to avoid erosion due to exessively high water velocities and since the water may flow between parts with different potentials, it must be deionized to keep it's conductivity down in order to prevent electrolyzing currents from dissolving the metal of the anode (Eddström, 1987).

- The busbars (1 and 8) are the conductors that carry power to and from the furnace. Large magnetic fields induced by especially the anode busbar may cause the arc to deflect from the vertical and it is for this reason that the anode busbar is installed as remotely as possible from the furnace to minimize magnetic field intensities that may cause the arc to deflect from the vertical. This is known as arc deflection and will be discussed in more detail in Section 2.3.1.

- In some processes the waste gas, such as CO in the ilmenite smelting process discussed in Section 2.2.4, is collected from the off gas port (8) where it is cleaned and scrubbed to remove the dust collected in the furnace. The gas is then used to preheat or dry reactants and the excess is flared into the atmosphere (Gous, 2006).

2.2.1 Plasma in the electric arc furnace and power control

The most important component in the electric arc furnace (EAF) is the plasma or arc which provides the necessary energy to realize the melting operation. In the dc EAF, the arc is initiated by electrode contact. As the electrode and furnace charge meet, a short circuit current is established that heats the contact point sufficiently for thermionic emission to occur. Consequently electrode material evaporates and is ionized, providing the initial charge carriers necessary to establish the arc. After a short period of electrode contact, the cathode is drawn away from the anode to a distance referred to as the arc length and the arc column is formed as illustrated in Figure 2.2.

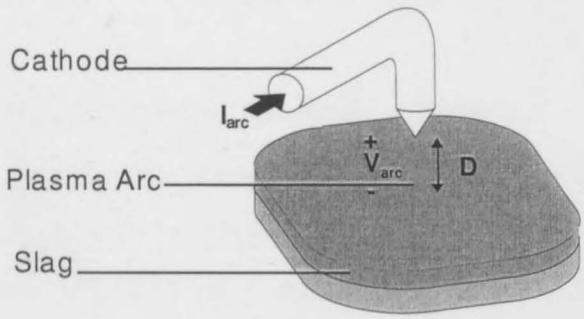

Figure 2.2. An illustration of arc length and the arc column in the electric arc furnace.

The EAF is supplied by a constant-current power source which will be discussed in more detail in Section 2.2.3. As the resistance of the arc, R_{arc}, varies, its voltage compensate so as to satisfy Ohm's law

$$V_{arc} = I_{arc} \times R_{arc} \qquad \text{Equation 2.1}$$

while the active power delivered to the furnace is given by

$$P = V_{arc} \times I_{arc} \qquad \text{Equation 2.2}$$

The resistance of the arc column is changed by varying the arc length, which in turn alters the voltage. Thus voltage control can be achieved by controlling the arc length. Together with current control this constitutes active power and hence thermal energy control in the EAF.

The dc EAF is more efficient in delivering its power to the furnace charge or melt when compared with the ac EAF and the dc plasma gun*. This is due to a convection phenomenon of the gasses surrounding the dc arc. These gasses are pulled into the arc and are directed down towards the melt by a natural convective pumping action. This characteristic of the dc transferred arc affords the dc EAF an overall 7% increased efficiency when compared with other electric furnaces (Edstrom et al., 1987; Maske et al. 1985). The dc plasma gun is supplied with a plasma gas that is more readily ionized, and which expands rapidly as it enters the plasma. The arc of a plasma gun is thus unable to pull in any surrounding gas and thus shows poorer efficiency than the dc arc furnace.

2.2.2 A Comparison between ac and dc furnaces

The conventional EAF is the 3 phase ac furnace referred to briefly in the previous section. It uses three graphite electrodes to strike arcs that deliver power to the furnace charge. Over the past three decades the dc furnace has gained increased popularity over the ac furnace due to its superior efficiency. Listed below are some distinct advantages the dc furnace holds over its ac counterpart:

- More efficient heat transfer from the arc to the anode. A strong electromagnetic plasma jet convects most of the heat from the graphite cathode to the furnace charge in a dc EAF. This leads to a 7% improvement in efficiency relative to the conventional ac furnace, as reported by (Kweyama et al., 2005; Edstrom et al. 1987).

- Longer and more stable arcs are generated in dc furnaces since arc re-ignition each half cycle is not required. Arc re-ignition occurs in ac furnaces due to the periodic switching of electrode polarities. This is not the case for the dc furnace and hence longer arcs can be achieved.

* The dc plasma gun differs from the dc EAF in that its arc is not transferred, but rather suspended between 2 electrodes above the melt with a resulting plasma tail flame that is projected onto the melt. At this point it becomes clear that the convention is to use the term *plasma* when making reference to the heating element in a nontransferred arc application, such as the dc plasma gun, and to use the term *arc* when referring to the plasma in transferred arc applications, such as in the dc or ac EAF.

Consequently the same power throughput is possible at a lower current and this reduces electrode consumption (Kweyama et al., 2005; Edstrom et al., 1987).

- Arc orientation is more symmetrical in the case of the DC furnace. The arc in an ac furnace burns at an angle since it forms part of the three phase system and hence is influenced by the magnetic fields generated by the adjacent arcs. This phenomenon of arc deflection causes dissymmetrical heat distribution on the furnace walls which in turn leads to increased wear and hence additional down time (Evers, 1999).

These advantages translate to increased profitability through an increase in furnace power efficiency as well as a decrease in furnace downtime required for necessary repair and maintenance.

The main disadvantages of dc furnaces, as reported by Knight et al. (1990), are:

- The initial capital cost of the power supply is greater.
- The generation of extra harmonics, by the power supply, as discussed in the following section. These harmonics are compensated for using appropriately tuned reactive filterbanks.
- The need for a return anode to close the electrical path. Consequently anode design forms a principal area of research and great advances have been made in the past twenty years.

2.2.3 The dc EAF power source

The dc EAF is supplied with power by a rectified power source that converts the 3 phase line – to - line currents, I_{ll}, to a dc current using a thyristor - driven power source. A practical circuit of a 3 phase to dc power source is presented in Figure 2.3.

During operation, the electrode occasionally touches the furnace charge. This results in short circuit currents that may last up to a few seconds. To limit the short circuit current and to stabilize the arc current, the power source is fitted with a dc reactor coil. This reactor also dampens the harmonics that are fed back to the power grid as a consequence of using a thyristor - triggered power controller.

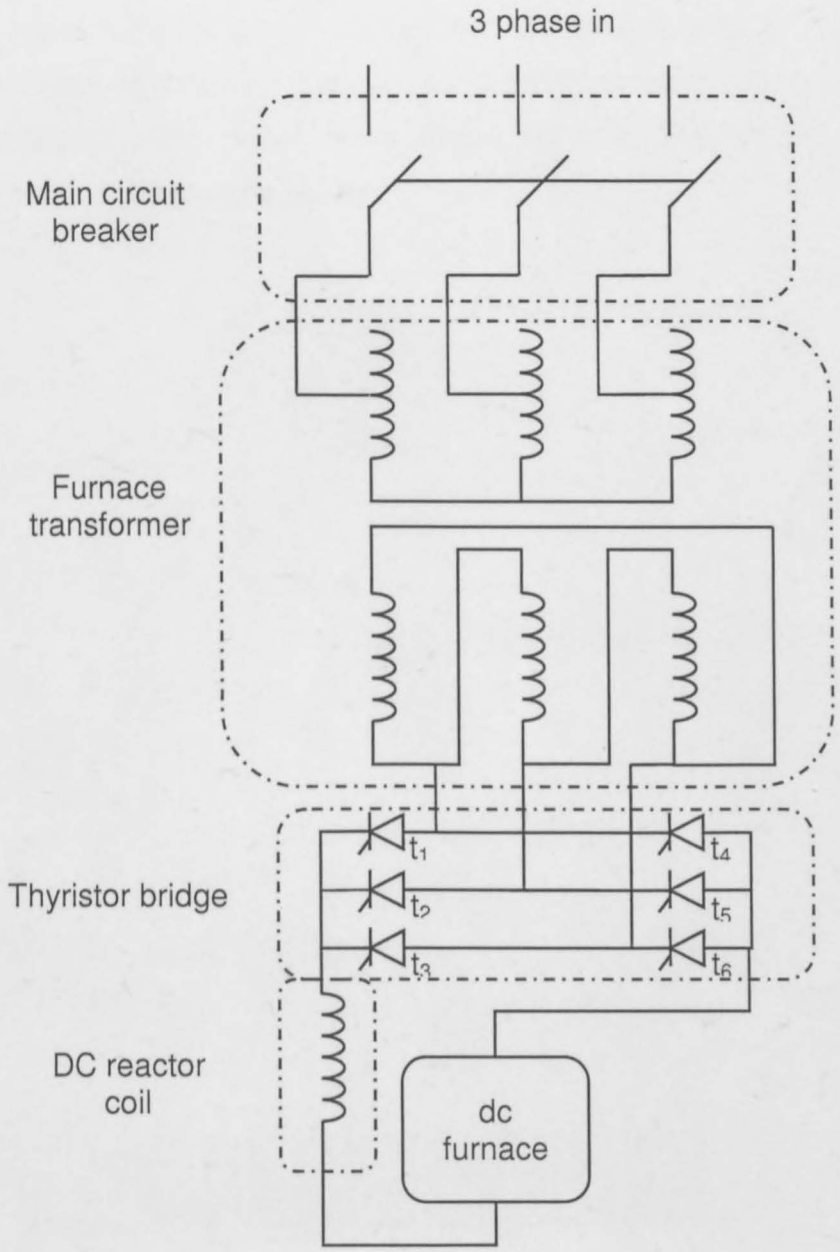

Figure 2.3. A practical dc EAF power source.

The 3 pairs of thyristors, t_1 to t_6, are controlled by a microprocessor triggering unit that supplies each with a gate current, i_g, which switches them into their on states. Thyristors are similar to diodes in that they only pass current in one direction (from anode to cathode), when a forward polarity exists. However, unlike a diode they also need to be triggered into an on state by supplying a gate current whilst there is a forward polarity (Mohan et al., 2003).

By applying gate current pulses that are delayed with an angle α (known as the delay angle or firing angle), current commutation can be controlled. This is illustrated in Figure 2.4, which shows the effect of 0, 30 and 60 degree delay angles on the dc side voltage.

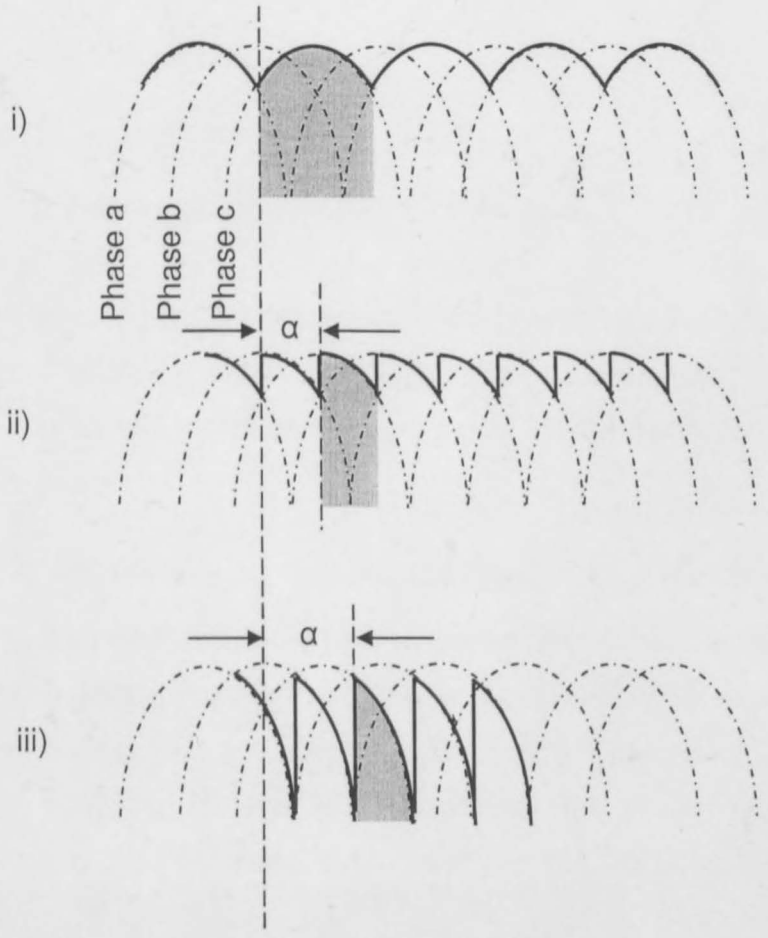

Figure 2.4. An illustration of how the commutation of current is controlled with a firing angle of i) 0° ii) 30° and iii) 60º.

The shaded area in Figure 2.4 represents the current commutation, when focusing on phase c by itself. We can see that phase c is passed only when it is triggered, i.e. when the delay angle expires, the corresponding thyristor - pair is provided with a gate current which switches it into an on state and in doing so the current is passed through it to the dc EAF. With a constant gate current (no delay angle as depicted in Figure 2.4, i) the thyristor bridge combination acts simply as a diode bridge rectifier. Thus by delaying the firing angle, the average dc current, represented by the bold line in Figure 2.4, is controlled.

The average dc side current and the power delivered by the thyristor bridge can be obtained using the following two equations (Mohan et al., 2003):

$$P = V_d I_d = 1.35 V_d I_g \cos\alpha \qquad \text{Equation 2.3}$$

$$I_{d\alpha} = 1.3 I_{ll} \cos\alpha \qquad \text{Equation 2.4}$$

where I_{ll} is the line to line voltage on the AC side.

As seen from Figure 2.4 the output of the power source contains harmonics at six times line frequency. In South Africa a dc furnace using a thyristor driven power source will therefore contain a 300 Hz fundamental component in its power supply.

2.2.4 DC electric arc furnaces in South Africa – Application

South Africa possesses extensive reserves of chromium and manganese ores and is a major producer of ferro-alloys. Considerable amounts of metal fines (small particles) that are less than 6mm in length are produced when cast slabs of ferrochrome and ferromanganese are crushed to meet the size requirements of customers. Even when the market is favourable these fines are sold at prices well below that of the larger particle sizes (25mm to 100mm). During unfavourable market conditions these fines cannot be sold at all and this represent a serious loss of revenue to the producer (Mc Rae et al., 1985).

The remelting of these fines are therefore necessary to convert them to a sellable product by effectively resizing the ferrochrome and ferromanganese and at the same time refining them. This is done in dc transferred arc furnaces that utilize a hollow cathode to deliver the feed directly into the hot spot of the furnace. This provides a close coupling between the furnace power and the process at hand, as well as allowing for the charge to be deposited directly into the bath since the arc holds the slag at bay.

At Namakwa Sands in the Western Capes, Ilmenite from beach sand is reduced with carbon (anthracite) to produce a Titania slag. This slag contains 86% of $Ti0_2$ and the process produces pig iron simultaneously with a carbon content of 2.5% (Gous, 2006). Like the ferrochrome and ferromanganese process discussed above, this is achieved using a single hollow cathode electrode and a dc transferred arc configuration. The high electrical conductivity of Titania slags and the accurate control of the Titania slag composition rules out the use of conventional submerged arc or inductive furnaces for this process.

2.3 The acoustics of an electric arc furnace

According to Babcock et al. (1968), plasma exhibits a fluid - like surface tension which acts as a membrane or diaphragm that can induce pressure waves in air or any gaseous medium. A periodic motion of plasma within the audible frequency range (20 Hz to 20 KHz) can therefore be heard. In this way plasma is very similar to a loudspeaker that utilizes an electromagnetically coupled diaphragm to produce sound from an alternating current.

This section is concerned with the literature that deals with plasma acoustics. In the electric arc furnace, two phenomena have been identified that cause the arc to move or deflect from the straight line that forms the shortest path between the cathode tip and anode. These phenomena are firstly, arc deflection, and secondly arc instability, and are considered in Sections 2.3.1

and 2.3.2 respectively. In Sections 2.3.3 and 2.3.4 the work of Babcock et al. and Nadau et al. is discussed, which investigates the use of plasma as an acoustic transducer and the relationship between an ac arc and its power.

2.3.1 Arc deflection in a dc EAF.

According to Evers (1999) the bus bar to the anode in a dc EAF contributes the largest magnetic field generated by the conductors in an EAF. This magnetic field acts on the arc and causes it to deflect from the vertical. This positional disturbance of the arc is known as arc deflection (Zweben et al., 2002).

The two laws that govern the current understanding of arc deflection are Ampere's law and the Lorenz law. Ampere's Law (Haus et al., 1989) is named after the French physicist André-Marie Ampere who is accredited as one of the main discoverers of electromagnetism. It permits the calculation of the magnetic field strength that surrounds a current carrying conductor and its differential form is given by

$$\nabla \times \mathbf{B} = \mu_0 \mathbf{J} \qquad \text{Equation 2.5}$$

where B is the magnetic flux density in teslas which quantifies the strength of the magnetic field, J the current density in A/m^2 and μ_0 is the permeability of free space. If we assume the conductors that carry the current to the furnace to be infinitely long straight wires, equation 2.5 reduces to:

$$\mathbf{B} = \frac{\mu_0 \mathrm{I}}{2\mathrm{r}} \qquad \text{Equation 2.6}$$

Here r is the distance in meters at which the magnetic flux density is measured and I is the current in the conductors. From equation 2.6 we can see that the strength of the magnetic field is proportional to the current, I, and inversely proportional to r. The direction of the magnetic field can be determined using the right hand rule. The magnetic field lines surrounding a straight current - carrying conductor are illustrated in Figure 2.5 below.

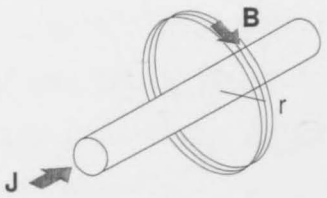

Figure 2.5. An illustration of Ampere's law.

To determine the force exerted on a charge in the presence of a magnetic field we use the Lorenz Law (Herman et al., 1989). Named after Dutch scientist Hendrik Antoon Lorenz, it describes the strength and direction of the force acting on an electrical charge in the presence of a magnetic field.

$$\mathbf{F} = q(\mathbf{E} + \mathbf{v} \times \mathbf{B}) \qquad \text{Equation 2.7}$$

Here F is the force exerted on the charge q, **v** is the instantaneous velocity of the charge and **E** is the electric field. In the case of the EAF the force acts on the arc which is composed essentially of ionized gas. We note that the magnetic field is perpendicular to both the charge and the velocity of the charge and we neglect the electric field **E** which has no influence on arc deflection since it acts only to accelerate the charge towards the metal bath. So equation 2.7 reduces to

$$\mathbf{F} = q\mathbf{v} \times \mathbf{B} \qquad \text{Equation 2.8}$$

Figure 2.6 for an illustration of the force exerted on a current carrying conductor in the presence of a magnetic field.

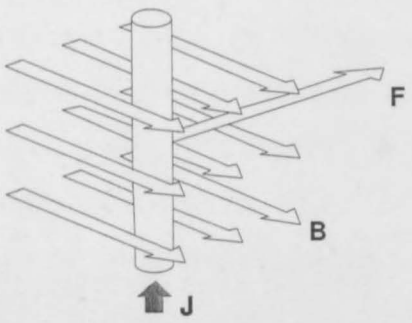

Figure 2.6. An illustration of the Lorenz law and the force exerted on the arc in the presence of a magnetic field.

It is relatively straightforward to calculate the strength and direction of the magnetic field surrounding conductors with simple geometric shapes. However, the magnetic field surrounding the complex conductors of an EAF is significantly more difficult and requires the assistance of software packages designed with this purpose in mind.

Some important relationships are presented by equation 2.6 and 2.8. First, it is evident that the magnetic force F is proportional to the length of the current carrying conductor (in the EAF this is the length of the plasma arc) as well as magnetic flux density B which in turn is proportional to the current through the conductor I_{arc}. Secondly, the direction of the magnetic force, F, is governed by the right hand rule as illustrated in Figure 2.6. Figure 2.7 illustrates how the arc in a dc EAF is deflected by the magnetic field in the vicinity of the anode and its bus bar.

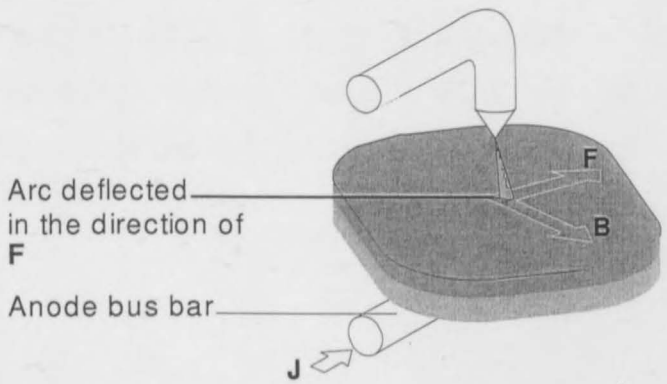

Figure 2.7. Arc deflection in an EAF.

In a set of experiments performed by Kang et al. (Kang, 2002) the dependence of arc deflection on initial arc length, magnetic field intensity and arc current of a welding arc was investigated. It was found that when a uniform magnetic field was applied to an ac arc or an alternating magnetic field to a dc arc, the arc would oscillate in the direction normal to the welding direction (i.e. the direction indicated in Figure 2.7). The weaving width of the arc and frequency is easily controlled by the magnitude and frequency of the applied arc current.

2.3.2 Arc Instability

When it comes to arc behaviour, the term "stability" refers to the observation of two phenomena which are only partly understood. Firstly, arc instability refers to any spontaneous fluctuation of the arc shape independent of any external arc deflection (Eddström, et al. 1987). Secondly, it refers to the seemingly erratic movement of the arc-cathode attachment spot, also called the arc root, during normal operation (Knight et al., 1990; Eddström, et al. 1987).

The first type of instability has a much more pronounced effect, causing undesirable "flicker" on the power grid that supplies the furnace which generates broad band noise, with frequencies from 50 Hz to above 1000 Hz (Zeben et al. 2000). In a set of experiments performed by Zweben et al., it was found that the onset of this more pronounced type of arc instability is dependent on arc current (I_{arc}), electrode separation and also cathode geometry. The movement of the arc column, whilst unstable, is most strongly influenced by the cathode geometry, as illustrated in Figure 2.8.

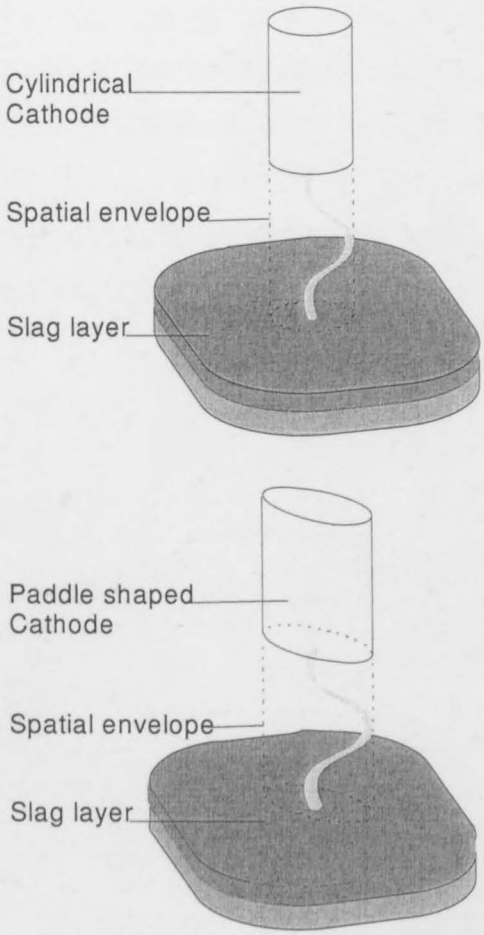

Figure 2.8. An illustration of how the arc movement is bounded by the geometry of the electrode during arc instability.

As seen in Figure 2.8, a paddle shaped cathode and a cylindrical cathode were found to allow only for motion of instability in a corresponding paddle shaped and cylindrical shaped envelope.

Knight et al. (1990) ascribes the movement of the arc root, the second type of instability, to convective and electromagnetic effects, as well as possibly the erosion of the electrode tip. In the Knight experiments arc instability was reported to increase with increasing arc current and to decrease with increasing arc length.

2.3.3 Plasmas used as acoustic transducers.

In a series of experiments performed by Babcock et al. (1968), a recording of Beethoven's Fifth Symphony was sounded using Acetylene-Oxygen plasma, see Figure 2.9. The quality of the reproduction was apparently limited only by the quality of the recording and modulating unit, which in this case was a magnetic tape cassette player. According to Dr. Cattaneo: 'generally the hotter the flame, the greater the ionization of the fuels...' and 'the louder and more faithful the sound reproduction.'

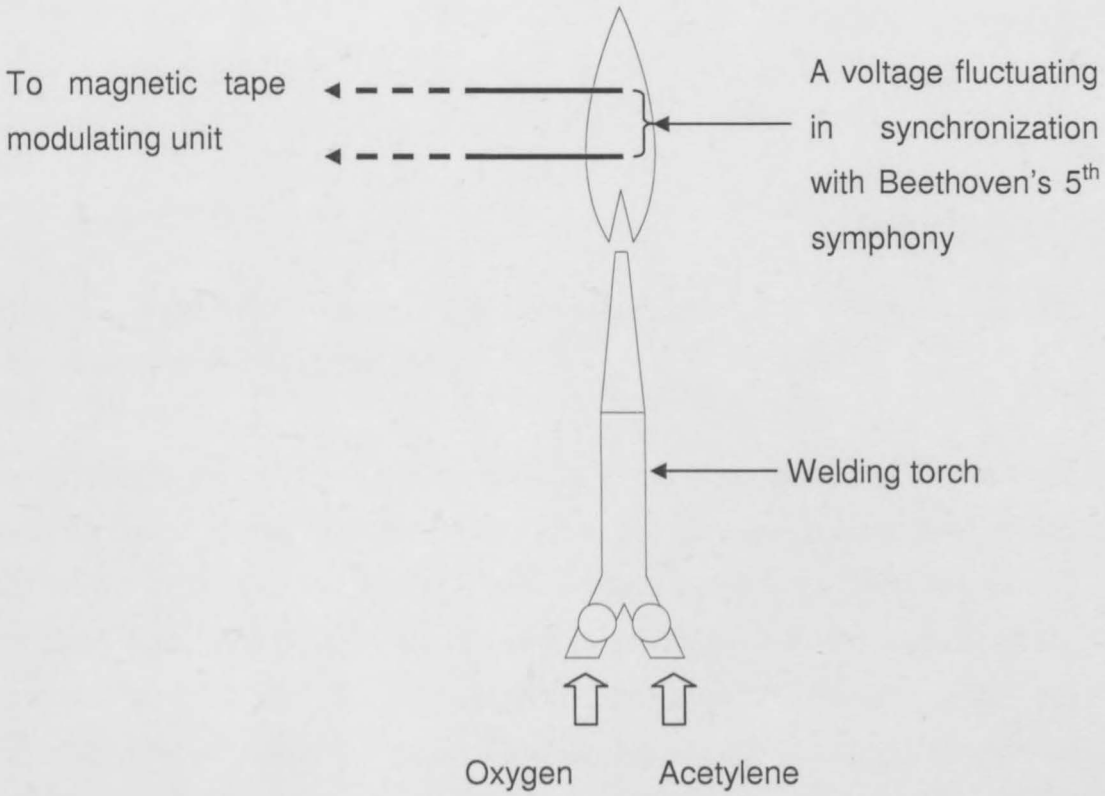

Figure 2.9. An Illustration of the experimental setup used in the Babcock et al. (1968) experiments.

Since the output of the modulating unit is a voltage that varies in accordance with the information contained on the magnetic tape, which under conventional circumstances would drive an acoustic transducer, the Babcock experiments indicated that a relationship exists between the plasma and the voltage across the plasma. This encourages one to speculate that a

relationship exists between the acoustics of a plasma and it's length at a constant current, since variable arc length at constant current implies a variable voltage across the arc, as described in Section 2.2.1.

2.3.4 The relationship between the acoustics and power of ac arcs

The work done by Drouget and Nadeau (1982) proposes the use of the acoustics of an ac arc to impose arc length and hence voltage control in ac arc furnaces. It was found that there exists a remarkable similarity between the time integral of the acoustic signal, S_a, and the time evolution of the arc power, VI:

$$S_a(t) = kV(t)I(t) \qquad \text{Equation 2.9}$$

with

$$k = \frac{\alpha(\gamma-1)}{c} \qquad \text{Equation 2.10}$$

where α is a geometric factor, γ the adiabatic expansion coefficient of air and c the velocity of sound in the arc.

To control the arc length of each electrode in the three phase ac furnace, the current in each phase must be compared to the the acoustic signal. A strong 120 Hz component in the sound would indicate some unbalance in between the three arcs. The 120 Hz component is in phase with the square of the current that runs through the electrode that needs to be adjusted: the corresponding electrode is hoisted if the signals are out of phase and lowered if they are in phase.

2.4. Summary

Over the past three decades, the South African Institute of Mineral Technology (Mintek) has invested much in developing and implementing technologies, which rely on the dc. This indicates that there exists a clear drive to invest in the dc EAF by the South African industry. This provides

incentive to search for ways in which the technologies which the dc EAF relies on can be improved. This project arose as a result of this need and investigates the possible existence of a relationship between the sound generated by an arc, in a dc EAF, and it length. Such a relationship could be used to develop an acoustic sensor to improve on current methods of power control in the dc EAF, which are often subject to inaccuracies.

Due to the fluid like surface tension, which causes the plasma to act as a membrane which induces pressure waves in air, an arc or plasma is capable of generating sound. Movement of the arc in the audible frequency range can therefore be heard and two phenomena, namely arc deflection and arc instability, have been identified as known causes of arc movement in the dc EAF.

The experiments performed by Babcock et al. (1968) indicate that there exists a relationship between the voltage across an arc and the acoustic signal generated by it. These experiments, together with those performed by Drouget and Nadeau (1982), which investigated the relationship between the power in ac arcs and the acoustics they generate, motivate the possible existence of a relationship between the length of the arc and the acoustics emanating from it in a dc EAF. Also, since the line frequency in South Africa is 50 Hz and a typical power source that supplies a dc EAF generates six times line frequency harmonics, the acoustic signals emitted from a dc EAF can be expected to contain a 300 Hz component.

Chapter 3

Data Acquisition

3.1 Introduction

This chapter presents the steps taken in acquiring the database used in the feature selection, signal analysis and classification steps that are described in subsequent chapters. We consider the equipment used, the experimental setup and procedure, the problems that arose during this process, and the resulting database.

3.2 Equipment

All experiments made use of a 60 kW dc electric arc furnace (EAF) developed by the Department of Process Engineering at the University of Stellenbosch (US). This EAF uses a transferred arc to deliver up to 500 A to the charge, which is loaded into the furnace via a replaceable crucible. Figure 3.1 presents a cross-section of the US EAF.

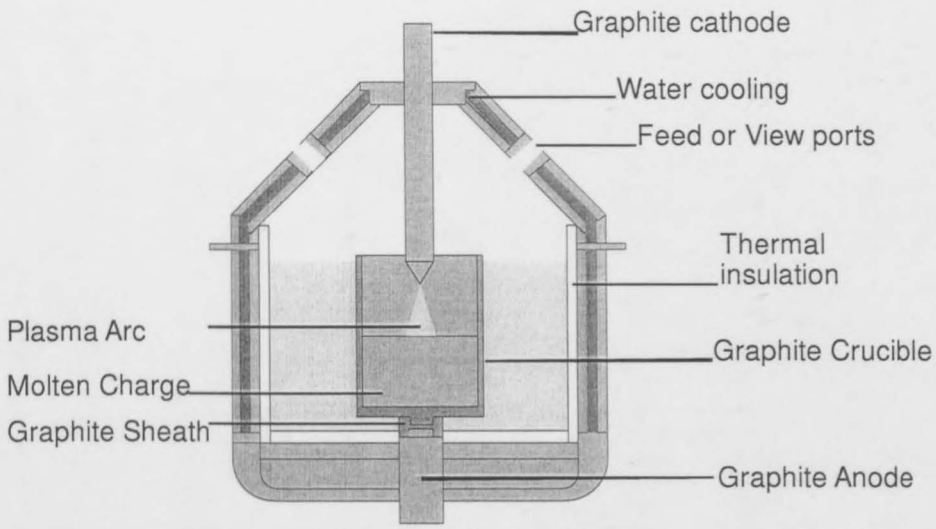

Figure 3.1. A Cross-section of the laboratory EAF used for experimentation.

The US EAF is similar in many aspects to the industrial furnaces presented in Chapters 1 and 2. However, there are a number of differences that make the US furnace better suited for laboratory use.

- View ports: Through these ports the operator is able, with the aid of protective eyewear, to view the inside of the furnace.
- Replaceable crucible: Unlike industrial furnaces, the US furnace is intended for use with various types of melts. It is thus necessary to use crucibles that are easily interchangeable and conductive to allow for closed circuit operation.
- Graphite Sheath: Due to the constant need to replace the crucible, the possibility of anode damage needs to be considered. A protective graphite sheath was developed that fits between the anode and crucible and can itself be replaced if needed.
- Fiber insulation material and alumina bubbles are introduced to provide extra protection for the furnace's inner walls against thermal damage, thus extending the lifetime of the furnace.

Figure 3.2 below provides an overview of the layout of the experimental setup.

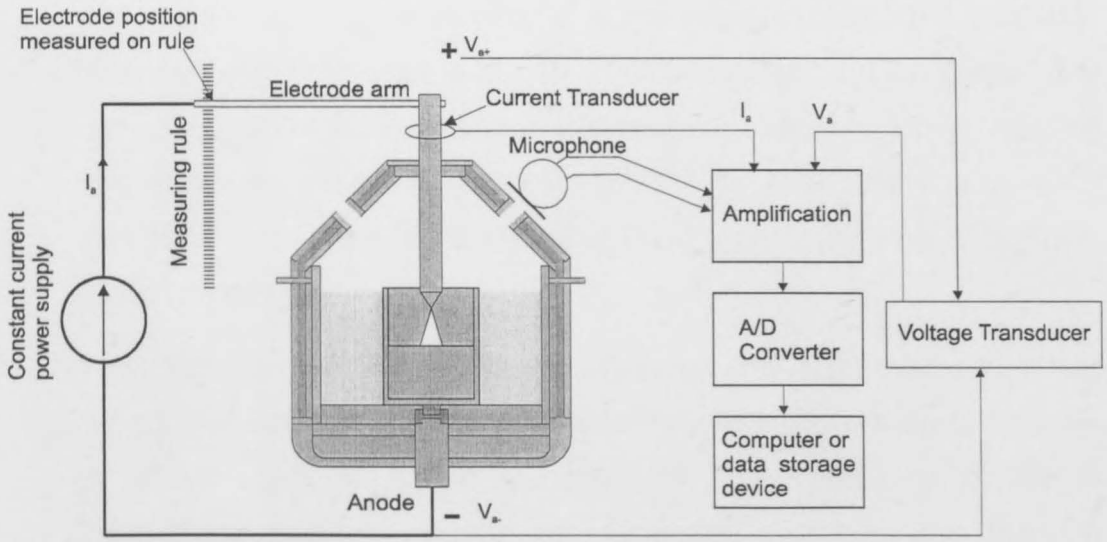

Figure 3.2. Experimental setup used to gather data.

The furnace is supplied by a constant current power source. A measuring rule behind the electrode arm allows the cathode displacement to be determined. By noting the electrode arm position when the cathode touches the anode (creating a short circuit which can be detected by monitoring the electrode voltage) and then adjusting the arm to hoist the electrode, the arc length can be set to the desired value.

The equipment used and their functions in the task of data acquisition are listed below:

- The microphone: This is the acoustic transducer that converts air pressure variations into a voltage for processing. The Samson C01 condenser microphone was used which has a flat frequency response over the 40 to 18000 Hz range.
- The preamplifier: The task of the preamplifier is to amplify the analog voltage signal obtained from the microphone to an amplitude of maximally ± 10 V so as to take full advantage of the resolution of the analog to digital (A/D) converter. The preamplifier is housed on the data acquisition unit (DAU) discussed below.

- A/D converter: This unit samples the analog signal obtained from the preamplifier and makes this digital signal available via a USB interface. The DT-9806 was used and has a 16 bit resolution with a maximum sampling rate of 50 kHz. The unit supports multiplexed inputs, dividing the maximum sampling rate between the input channels (e.g. when sampling 2 channels, a maximum of 25 kHz sampling rate is available per channel).

- Portable storage device: The A/D converter only samples the incoming signal and there is still a requirement for a memory device to hold the information captured by the A/D converter. The experiments performed here made use of a laptop computer that interfaces with the A/D converter and supplies it with power via a USB port. All data are stored and transported on the computer and then transferred to a PC workstation for further processing

- Voltage transducer (VT): This device isolates and divides voltages in the range of 10 to 1500 V by a set ratio, thus protecting the sensitive measuring equipment. The device I used here is the LV 25-P/SP2 developed by *LEM* and can process AC, DC and pulsed voltages.

- Current transducer (CT): This device allows the measurement of high currents up to 1 kA. The CT I used here was the LF 1005F-S, also developed by *LEM*.

- Data acquisition unit (DAU): To integrate the system a data acquisition unit was designed using computer package called PCAD. Figure 3.3 shows the layout of the module and the components that interface with it. The schematic and printed circuit board (PCB) layout for the prototype DAU can be found in Appendix A.

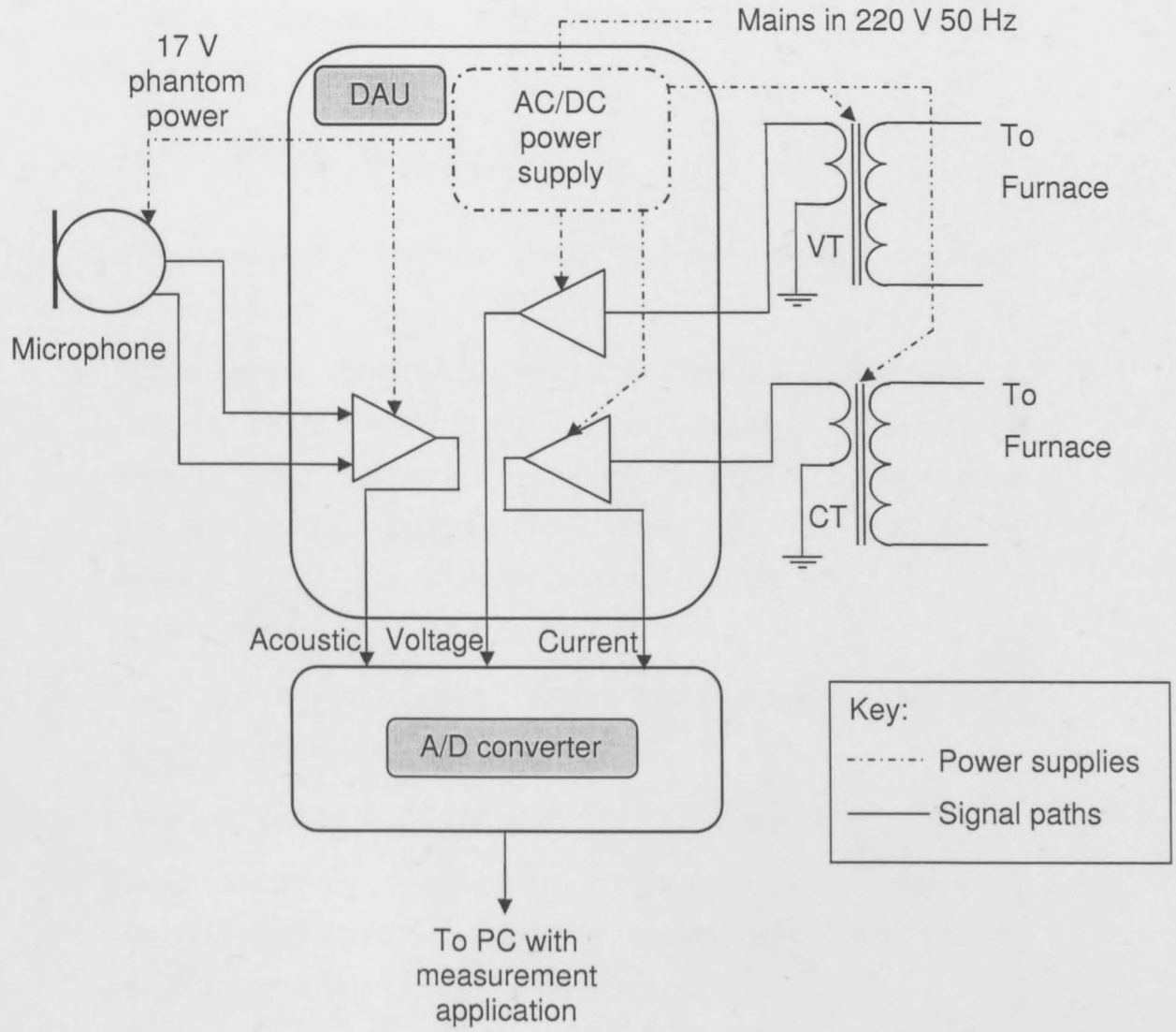

Figure 3.3. The data acquisition unit (DAU) and components that interface with it.

- Recording application: A graphical user interface application (measurement application or MA for short) was developed using the *DT Measure Foundry* package supplied with the A/D converter to assist with all signal recordings. The MA allows us to view all channels in the A/D converter's buffer once filled and to store the buffer on the laptop if so desired.

- Furnace power supply: The furnace supply is a 60 kW six pulse thyristor supply. It acts as constant current source and the current throughput to the furnace is directly controlled by adjusting a turn knob on the supply.

3.3 Experimental procedure

The following sequential procedure was followed for each individual experiment:

1: Before furnace operation, the charge is prepared, making sure that each individual particle is small enough to allow for proper arc initiation. If the particles are too large, they stack inside the crucible with open spaces between them, which can prevent proper arc initiation. Trial experiments showed a particle volume of approximately 1 cm^3 to be adequate.

2: The charge is then weighed to ensure that consistency is maintained during separate runs.

Once the charge is prepared, the preparation of the furnace begins:

3: Before commencing I ensure that the power supply is turned off at the mains and that the cooling water bypass valve is open (thereby not allowing water to flow to the furnace).

4: The electrode is hoisted up so that its does not encumber the removal of the roof.

5: The roof is removed and placed on a stand next to the furnace.

6: All debris (used fiber lining, used alumina bubbles and anything else) is removed from the furnace. Dust and all small debris are collected using a vacuum cleaner.

7: The viewing ports are removed from the furnace, cleaned and replaced.

8: Glass fiber lining is cut and fitted to line the inside of the furnace in order to protect the inner walls and bottom from splashing, as well as to provide thermal insulation.

9: The top of the anode is dusted with a small amount of graphite powder to aid conduction by increasing the contact surface between it and the graphite sheath.

10: The graphite sheath is now inserted into the notch in the anode and care is taken to ensure it is securely in place.

11: Again, and for the same reasons as mentioned in step 9, the top of the graphite sheath is dusted with a small amount of graphite powder.

12: The crucible is inserted into the notch in the graphite sheath, making sure it fits securely.

13: The volume surrounding the crucible is now filled with alumina bubbles (2 mm diameter alumina balls) to provide additional insulation.

14: The roof is placed back onto the furnace making sure it is securely fitted.

15: The cooling water bypass valve is closed to allow water to flow to the furnace and care is taken to ensure that all the remaining valves are in the open position and the water is flowing freely through the system.

16: The power source is turned on at the mains and an appropriate low current setting is selected to avoid crucible cracking due to thermal shock.

17: Whilst looking into the furnace with protective eyewear, the electrode is lowered until it is 3 cm above the contact surface.

18: The electrode is lowered whilst looking away from the furnace until a short circuit (contact with the furnace charge) is established. This is

confirmed by the voltage reading on the power source, which drops to almost zero.

19: The electrode is now hoisted by approximately 2 cm. The arc is now established.

20: After establishing the arc, 20 minutes are allowed to pass for the charge to melt completely.

21: The electrode arm is now lowered to establish the short circuit reference point which is noted, with the measuring rule as indicated in Figure 3.2, as 0 arc length.

22: The measurement application is turned on and set the directory to which the data are written.

23: The current setting is adjusted to the desired experimental level and the electrode arm is hoisted to the desired arc length.

24: At this point the first recording of the experimental run is made.

25: After making the first recording, the electrode is hoisted to the next desired arc length and the file name is adjusted on the MA for our next recording.

26: After all the recordings have been taken, the power source is switched off and the cooling water is left to circulate for a further 30 minutes to allow the system to cool down properly.

This sequence is followed for each experimental run, in addition to the safety procedures which were meticulously followed as demanded by the Faculty of Engineering. Each individual run takes approximately 1.5 days to complete, when there are no complicating factors.

3.4 Database design and results

To meet the outcomes identified in Chapter 1 it is important to use only data samples that are representative of 'normal' and steady - state operating conditions. That is, for this study acoustic recordings that included signal

anomalies such as stray arcing and arc instability, identified by a sharp whistling sound in the acoustic signal (Zeben et al., 2000), have been omitted. Recordings in which the arc exhibited the dynamic behaviour associated with melt-down, characterized by varying voltage and current levels, were also omitted. This is achieved by visually inspecting each A/D buffer before committing it to memory. Dynamic behaviour and arc instability captured during experimentation are shown in Figure 3.4 and Figure 3.5 respectively while Figure 3.6 shows a recording of a 10 mm arc that forms part of the final database.

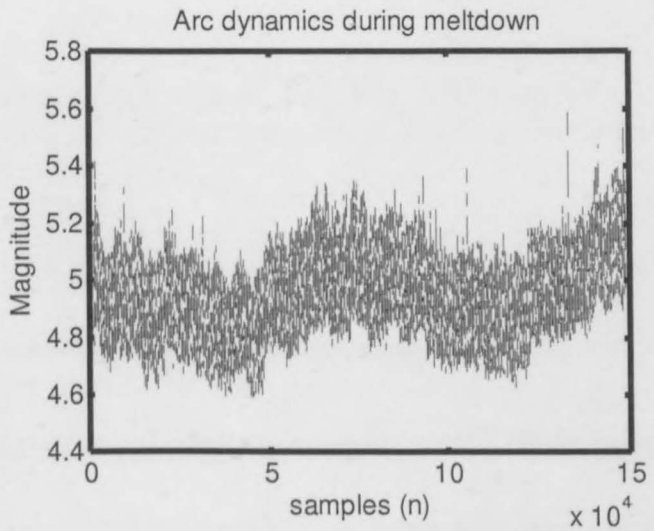

Figure 3.4. A voltage signal recording that displays the dynamic behaviour associated with the melt-down process. This recording, together with the corresponding acoustic and current recordings, consequently does not form part of the final database.

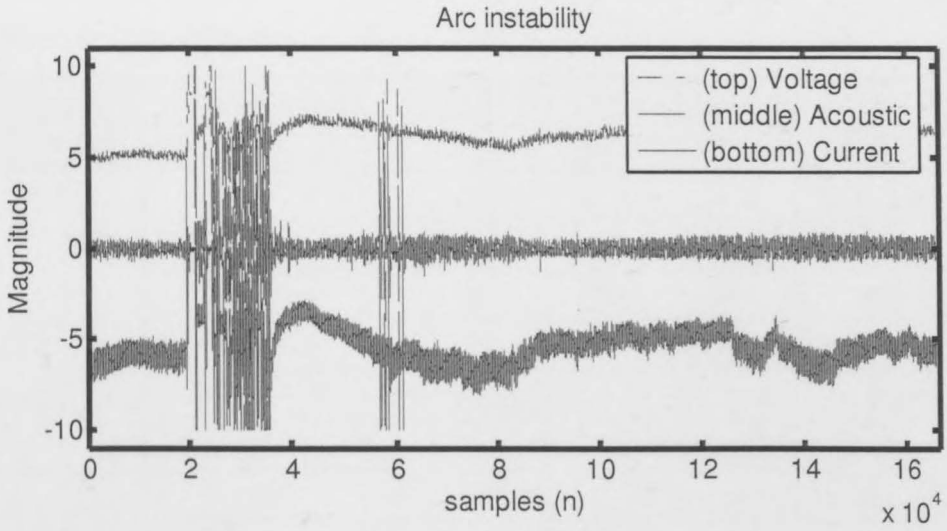

Figure 3.5. A recording which displays arc instability. This recording consequently also does not form part of the final database.

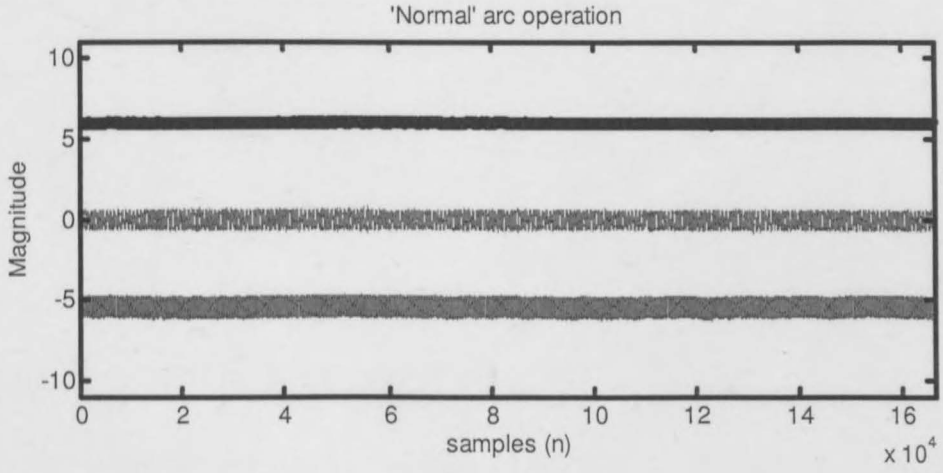

Figure 3.6. A recording that is free of dynamics and arc instability and which is therefore committed to the final database.

As can be seen in Figure 3.4 to Figure 3.6, each experimental recording consists of a 10 second recording of the acoustic, voltage and current signals, each sampled at 16 667 samples per second. During each run a charge of approximately 600 g of mild steel is used as melt. Recordings are made with the arc length increased in 5 mm increments from 5 mm to 30 mm.

The database was obtained over 7 separate runs and an overview of it is presented in Table 1 below.

Current	Arc Length (mm)	Number of runs	Total time recorded	Size (MB)
Low	5	7	70	65.87
	10	7	70	65.87
	15	7	70	65.87
	20	7	70	65.87
	25	5	50	47.05
	30	5	50	47.05
Medium	5	4	40	36.64
	10	4	40	36.64
	15	4	40	36.64
	20	3	30	28.23
	25	3	30	28.23
	30	2	20	18.82
High	5	2	20	18.82
	10	2	20	18.82
	15	2	20	18.82
	20	2	20	18.82
	25	2	20	18.82
	30	2	20	18.82

Table 1. Details of recorded database.

Each experimental run was intended to consist of recordings made at low, medium and high current settings. However, as seen in Table 1, this was only achieved in 2 separate runs due to experimental complications which are discussed in the following section.

Some initial experimental runs were also performed to investigate the influences of electromagnetic noise that is induced in the system, to calibrate the equipment and to inspect the bandwidth of the acoustic signal. However these were only intended to establish confidence in the system and do not form part of the database. In total, approximately 12 months were devoted to

the compilation of the database. This includes design, construction, testing and calibration of the measuring equipment.

3.5 Troubleshooting

Due to the novelty of these experiments, the laboratory EAF was used in a way not initially considered during its design. This caused several problems, and often experimental runs were abandoned for safety reasons or to ensure that experimental design parameters were kept consistent. These problems are discussed in the following sections to allow for a better understanding of the database.

3.5.1. Crucible lift

During an experimental run it was often necessary to re-establish the reference point of zero arc length. Great care is taken not to immerse the electrode tip in the melt, but nonetheless it often occurs. When this happens the melt can solidify and bond to the electrode. With the electrode and melt joined, they are lifted together with the crucible when the electrode is raised to establish an arc. This causes the insulating alumina bubbles to move into the space below the crucible, thereby obstructing the electrical path. Figure 3.7 presents an illustration of this situation.

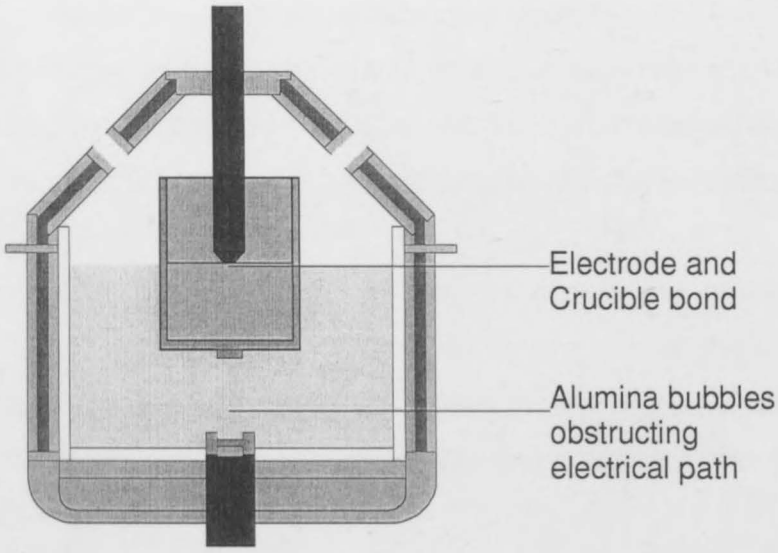

Figure 3.7. An illustration of crucible lift.

In the case of *crucible lift*, the furnace is switched of and left to cool down before opening it up and separating the electrode from the crucible. It was always possible to separate the electrode from the melt and thus the subsequent experiment was setup using the same crucible. However, *crucible lift* caused a delay in the data acquisition process of approximately one day each time it occurred, and happened frequently (approximately one in every two experiments).

3.5.2 Crucible cracking

Crucible cracking is a problem that arises due to the degradation of the crucible, which occurs as a result of the intense heat. At a certain point, the melt breaks through the side of the crucible and a crack originates from this point. When this situation arose, the experiment had to be aborted, the furnace left to cool and a new experimental setup prepared. This would cost the process about a day of effort and happened four times.

3.5.3 Water leaks

The water that cools the furnace enters at the top through a valve in the roof and exits the furnace through a valve at the bottom. The various valves that

transfer the water throughout the furnace often begin to leak. It is assumed that this happens because of the expansion and contraction of the furnace's metal components due to the heating and cooling cycles that it undergoes. Also, on occasion the water pipe that supplies the furnace would develop a small hole due to pressure and heat, and consequently water would leak out.

Water that comes into contact with the melt is considered to be a very dangerous situation. At the extreme temperatures of the melt the water can expand very rapidly and in the contained space provided by the furnace an explosion is a real possibility. It is for this reason that great care was taken not to allow any water leaks to develop.

Water leaks were detected often, however in most cases only an hour was required for repairs. On two occasions the water supply pipe burst, causing water to spray in all directions. This damaged the microphone, which then needed to be replaced. Furthermore, the laboratory had to be shut down for a period of one week, due to the extent of the flooding.

3.6 Summary

The original design of the US dc EAF did not take into consideration the aspects unique to the experiments performed in this study. This proved problematic and the data acquisition process suffered many setbacks. However, an adequate database of voltage, current and acoustic signals was obtained and is presented as partial fulfilment for this project. Also, a data acquisition system was developed to record and assess during run time the laboratory furnace's voltage, current and acoustic signals.

Chapter 4

Methodology

4.1 Introduction

According to Theodoris et al. (2004) pattern recognition (PR) is the scientific discipline concerned with the classification of objects into a number of categories or classes. Depending on the application, the objects may be images, signal waveforms or any type of measurement that needs to be classified. In the context of this project the objects are the recordings of the acoustics generated by a dc EAF and the classes or categories are the arc lengths of 5, 10... to 30 mm. More specifically this project seeks to identify similarities in data recorded at identical arc lengths with the aim of training models that are capable of classifying the arc acoustic recordings into classes that represent the various arc lengths at which the recordings were taken.

In practice various methods are employed to fight augmented deviations of the arc from its centre line (Edström et al., 1987). These augmented deviations are known as arc instability and were discussed in some detail in Chapter 2.3.2. Even without the presence of instability there is always a degree of movement of the arc attachment spot (Zweben et al., 2002), and hence an arc length of 5 mm represents the arc length setting and not the actual arc length fluctuating around that setting. The PR approach undertaken here was therefore a classification task, where data were classified to a discrete set of arc lengths or classes $w_i \in \{w_1, w_2, w_3, w_4, w_5, w_6\}$, as opposed to regression that is concerned with continuous outputs.

Figure 4.1 outlines the basic methodology followed during this project, and which follows closely the traditional pattern recognition approach.

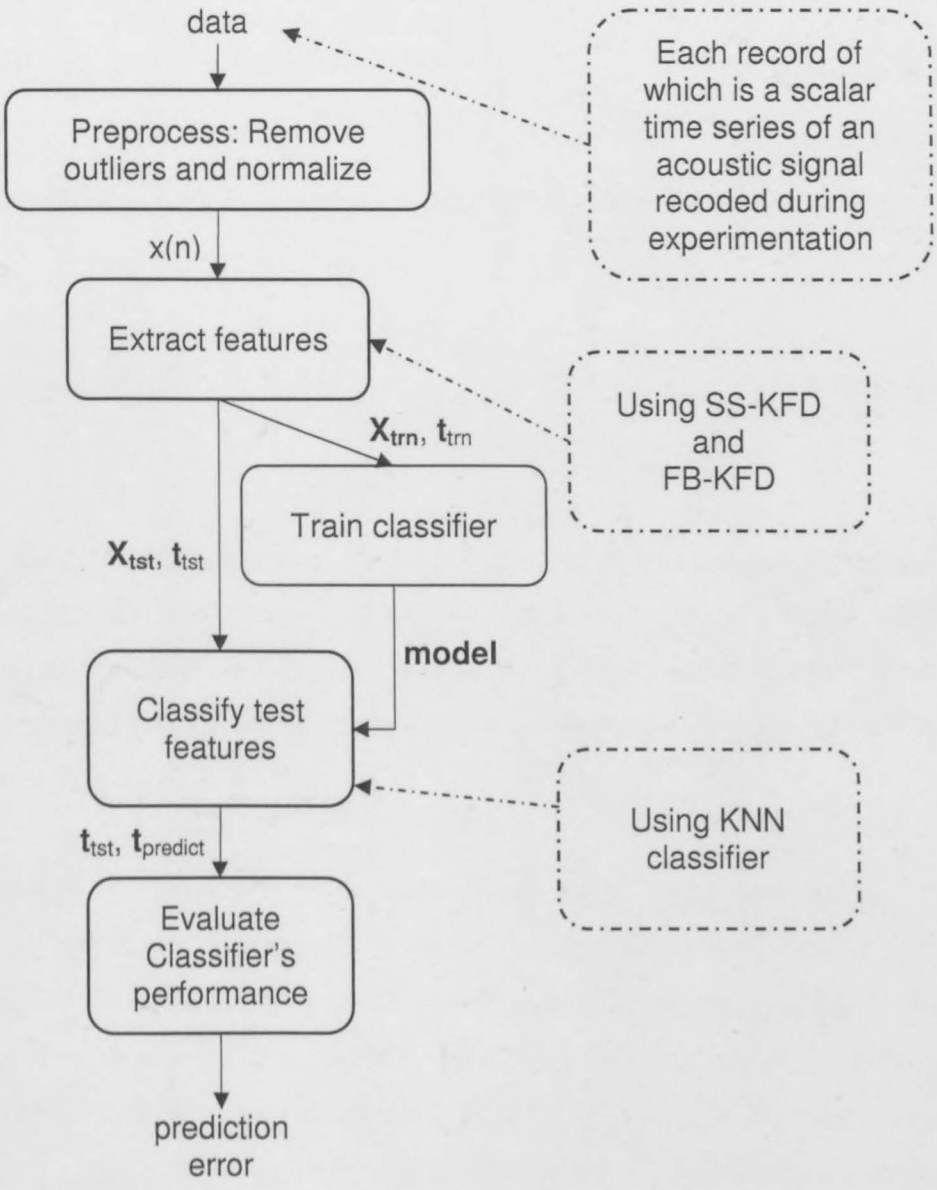

Figure 4.1. The pattern recognition methodology undertaken in this project.

The acoustic recordings are preprocessed to remove outliers and to normalize to zero mean and unit variance, as described in Chapter 4.2. The resulting time series, x(n), are then split into test and train data from which features are extracted to produce the feature matrices $\mathbf{X}_{trn}$ and $\mathbf{X}_{tst}$ respectively. These matrices contain the appended feature vectors, which define uniquely the

patterns in the data, of all the classes. For instance $\mathbf{X}_{trn}$ is constructed as follows:

$$\mathbf{X}_{trn} = \begin{bmatrix} \text{feature vectors from class 1} \\ \text{feature vectors from class 2} \\ \vdots \\ \text{feature vectors from class 6} \end{bmatrix} \qquad \text{Equation 4.1}$$

The train data, $\mathbf{X}_{trn}$, together with a corresponding target vector,

$$\mathbf{t}_{trn} = \begin{bmatrix} 1 \\ 1 \\ 2 \\ 2 \\ \vdots \\ 6 \\ 6 \end{bmatrix} \qquad \text{Equation 4.2}$$

that identifies to which class each corresponding feature vector belongs are then used to train a classifier model. This is known as supervised learning which can be defined as machine learning that uses labelled data. In other words supervised in the sense that we tell the algorithm which train samples belong to which class.

The methods employed in the feature extraction step are State Space reconstruction (SS) discussed Chapter 4.3.1, Filterbank Analysis (FB) discussed in Chapter 4.3.2 and Kernel Fisher Discriminant Analysis (KFD) presented in Chapter 4.3.3 and 4.3.4. To obtain the features evaluated in the classification step the two combinations of SS-KFD and FB-KFD were used in this project, the results of which are discussed in Sections 5.2 and 5.3 respectively.

After the feature extraction step a classifier model is used to label the test data, producing $\mathbf{t}_{predict}$, and in doing so effectively predicts to which class each test feature vector belongs. To evaluate the performance of the feature extraction and classification procedures, the actual classes of the test data, as labelled by $\mathbf{t}_{tst}$, are compared to the predicted classes of the test data, $\mathbf{t}_{predict}$.

The classifier chosen for this project is the k Nearest Neighbour classifier that is discussed in Chapter 4.4.

4.2 Preprocessing

Preprocessing consisted of two steps, namely normalization and outlier removal. These are described in the following two sections.

4.2.1 Normalization

The data collected in this database have dynamic ranges that differ with each experimental run, since each run is subject to unique conditions as dictated by the setup on the corresponding day. If left as is, the variance in dynamic range may influence the results of the feature extraction and classification steps that follow. This problem is overcome by normalizing the data so that all data lie within the same range.

Each acoustic time series is normalized with respect to the energy in the complete series. This is achieved by subtracting the mean, μ_x, from each time series $\mathbf{x} = \{x_1, x_2, x_3, \ldots x_N\}$ and dividing by its standard deviation, σ_x. Or more formally:

$$\hat{x} = \frac{x - \mu_x}{\sigma_x} \qquad \text{Equation 4.3}$$

where $\hat{\mathbf{x}}$ is the normalized time series, μ_x the sample mean:

$$\mu_x = \frac{1}{N}\sum_i^N x_i \qquad \text{Equation 4.4}$$

and σ_x is the sample standard deviation:

$$\sigma_x = \sqrt{\sum_i^N (x_i - \mu_x)^2} \qquad \text{Equation 4.5}$$

In Figure 4.2, the differences in dynamic range fluctuations before and after normalization are illustrated. The figure plots the appended recordings of 5 runs at the same arc length.

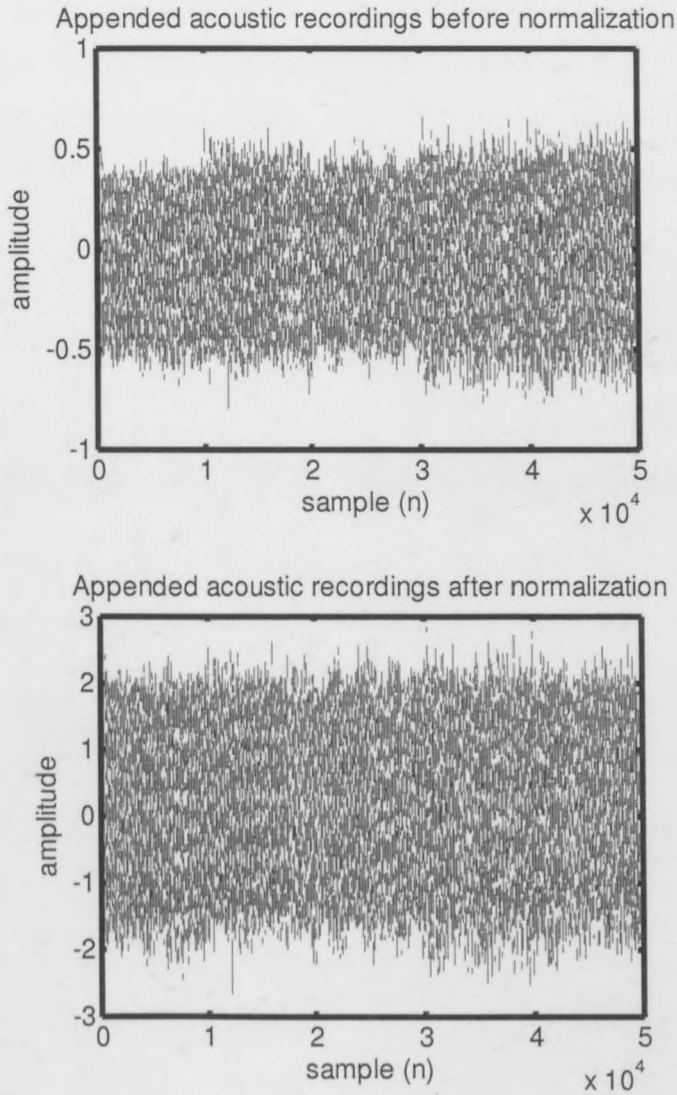

Figure 4.2. Appended acoustic recordings taken at 5mm arc length before (above) and after (bottom) normalization, where each of the 5 runs contains 10 000 samples.

4.2.2 Outlier removal

An outlier can be defined as any point that lies significantly far from the mean of the corresponding random variable (Theodoris et al., 2004). We assume that the data are normally distributed, and identify outliers as those samples that lie more than 3 times the standard deviation away from the mean. This identifies roughly 1% of the data as outliers.

During data acquisition, where possible, recordings containing outliers were avoided. However, occasionally a recording was partially corrupted with severe stray arcing or arc instability (as described in Chapter 3). Figure 4.3 shows an excerpt from a 5mm arc recording as well as its detected outliers.

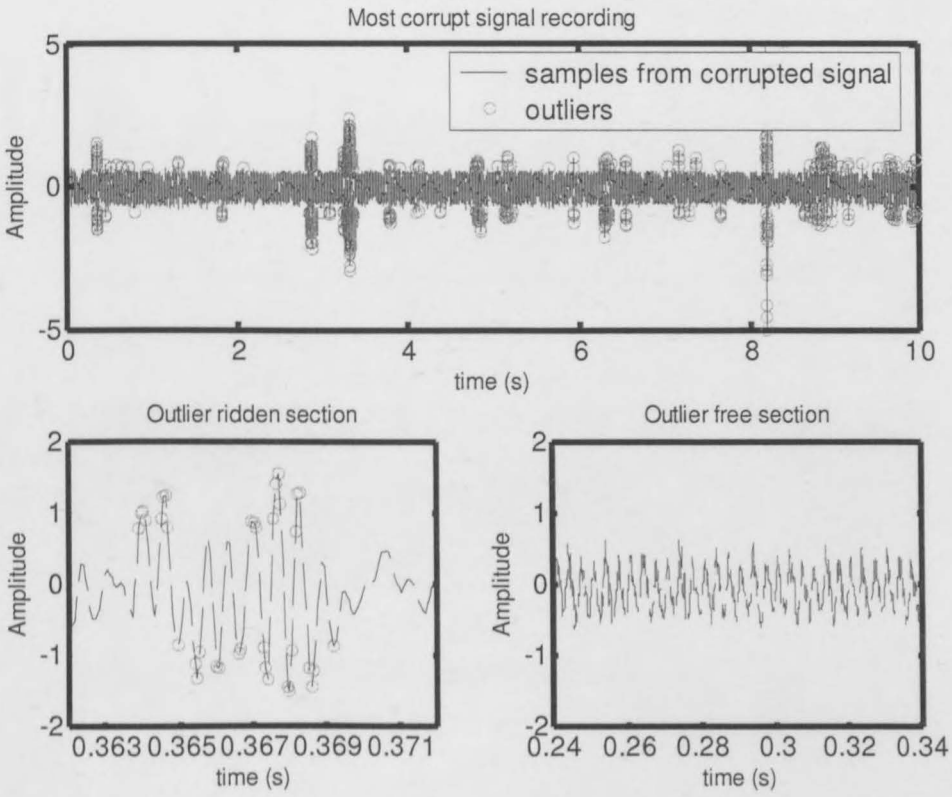

Figure 4.3. An excerpt from a 5 mm arc recording that shows detected outliers. The outlier - ridden sections (bottom left) are avoided during feature extraction whilst the outlier free sections (bottom right) are used.

In comparison with the rest of the database, this recording was particularly corrupted with acoustic anomalies. If left as is and samples that include outliers were used in the subsequent step of feature extraction, it may have had an adverse effect on the results, since the outliers do not represent the normal operation of the furnace which was the focus of this study.

To verify that the signal characteristics deviate substantially when outlier samples are detected, I used the spectrogram or Short Time Fourier Transform (STFT), as shown in Figure 4.4.

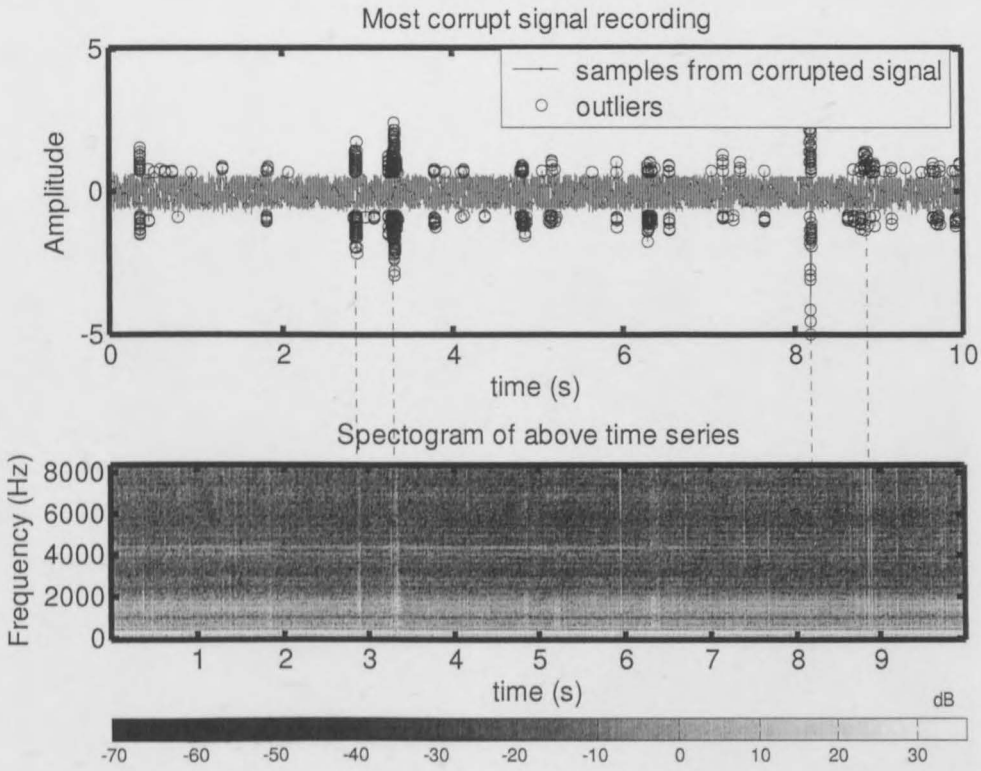

Figure 4.4. The time series (above) and spectrogram (below) of an outlier corrupted signal. The vertical dashed lines, connecting the top and bottom figures, illustrate the relationship between outliers in the signal and broad band energy in the spectrum of the signal.

The spectrogram is a time - frequency plot that presents the power spectrum of a signal at localized time instances (time against frequency against amplitude), as opposed to a normal Fourier analysis in which the time locality is lost (frequency against amplitude). In Figure 4.4 above we can see vertical bands of energy corrupting the power spectrum (represented by the colour gradient) at each instance of an outlier.

It is apparent from the spectrogram in Figure 4.4 that the bandwidth of the signal increases where outliers are detected. The broadband energies may be

attributed to the 'clipping' effect caused by a sample that lies beyond the range of the A\D converter (see Chapter 3.2). This causes a sharp discontinuity in the signal and corresponding broad band frequency content in the power spectrum. However, the outlier samples cannot merely be discarded individually as can be seen in Figure 4.5 below, where the outliers were omitted from the signal.

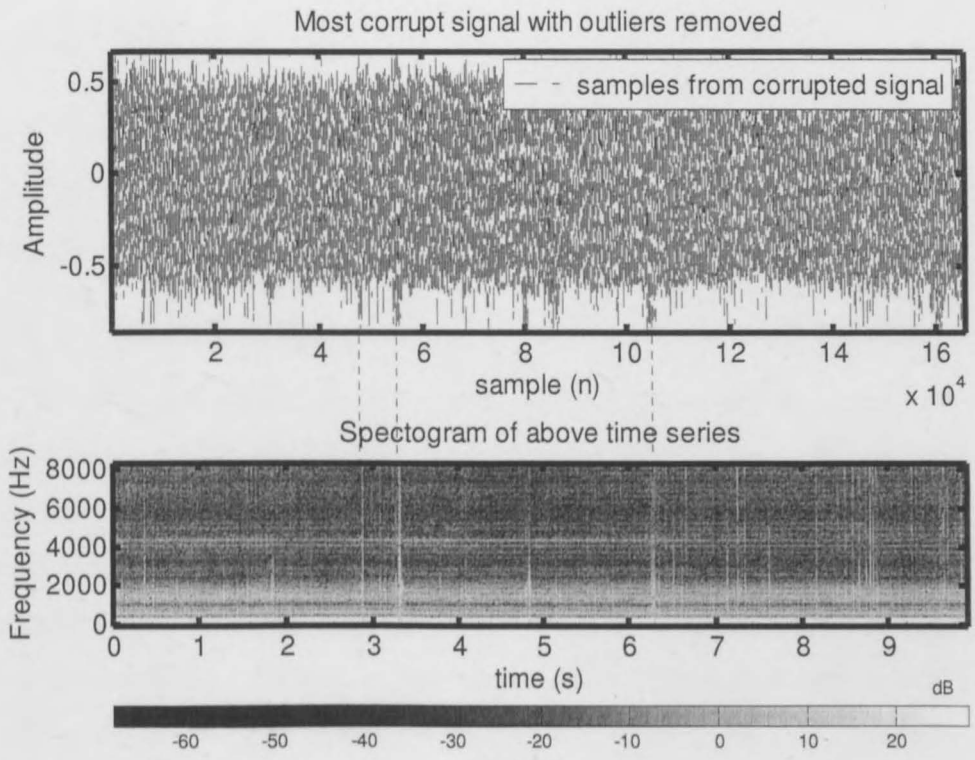

Figure 4.5. Time series of the most corrupt signal (above), with outliers removed by omission, and its spectrogram (below). The vertical dashed lines indicate that the omission of the outliers had not removed the broad band energies in the signal's power spectrum.

The vertical energy bands in the spectrogram indicate the presence of broad band energy at the locations at which the outliers were present. The persistence of these broad energy bands in the spectrogram may be due to the discontinuities induced into the time signal - domain signal by removing individual samples. However, they may also indicate that a wider margin of

samples neighbouring the outliers should be considered abnormal and removed from the signal.

Instead of including such heuristics in the methodology followed here, the train and test data were simply extracted from outlier free portions of the recorded signal, portions like the one shown in Figure 4.3 (bottom right). This limited the usable sample lengths to 10 000 consecutive samples.

4.3 Feature extraction

Feature extraction refers to the generation of descriptors or features that compactly describe the information in a signal. The following sections describe the feature extraction approaches used in this study.

4.3.1 State Space reconstruction

To allow the use of multivariate analytical methods, such as Fisher discriminant analysis (FDA), the one dimensional acoustic time series was embedded into a higher dimensional space. According to Takens (1981) the underlying dynamics of a nonlinear system can be understood, and its geometrical behaviour generalized, by observing the time delay vectors of a time series. This principle is known as state space reconstruction. The first point of decorrelation, when inspecting the auto correlation function (Figure 4.6 below) of a typical acoustic recording, was observed to be at a lag of approximately 14.

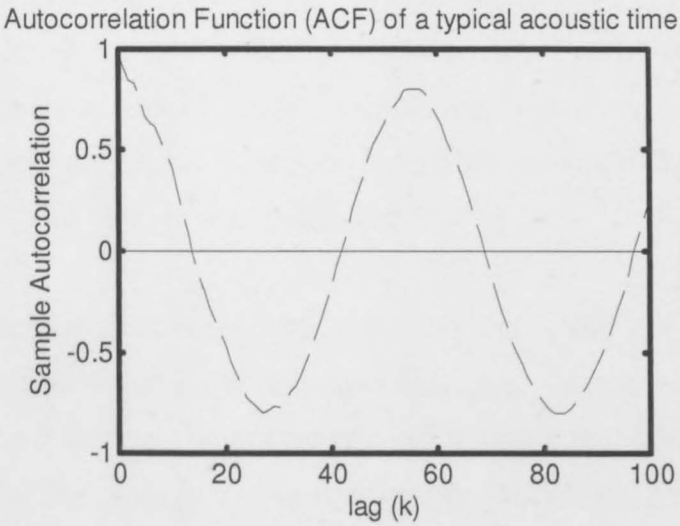

Figure 4.6. The autocorrelation function of a typical acoustic recording.

An embedding dimension, d_e, of 15 was therefore used, this includes the zero lag or original time series, and a time lag, τ, of 1. Thus the acoustic time series was imbedded into its state space reconstruction as follows

$$\mathbf{X}_{ss} = \begin{bmatrix} x(1) & x(2) & x(3) & \cdots & x(d_e) \\ x(2) & x(3) & \vdots & & \vdots \\ x(3) & \vdots & & & \\ \vdots & & & & \\ x(N) & x(N+\tau) & \cdots & & x(N+d_e) \end{bmatrix} \quad \text{Equation 4.6}$$

Where $\mathbf{X}_{ss}$ is the state space reconstruction of the time series x(n) with length N and the embedding dimension of d_e equal to 15.

4.3.2 Filterbank Analysis

The Filterbank (FB) analytical technique is most popularly used in the Mel frequency cepstral coefficient algorithm (MFCC), which is used to extract features for automatic speech recognition. The MFCC algorithm uses nonuniformly spaced filters and the discrete cosine transform to extract features that are relevant to human auditory perception, which is most sensitive in the sub 10 kHz range (Skowronski., 2003).

The FB employed here, however, comprised a set of uniformly spaced band pass filters (BP), as opposed to the nonuniformly spaced triangular filters used in MFCCs. These bandpass filters - with frequency responses of $H_0(f)$, $H_1(f)$, ...$H_k(f)$ – was arranged in parallel to split the frequency spectrum of a time series, x(n), into subbands. The subbands were then sub-sampled into frames and the energy of each frame calculated.

Figure 4.7 illustrates how the filterbank algorithm splits x(n) into a number of 512 sampled frames and calculates the energy contained in each. The energy denoted E_{11} is therefore the energy of the first frame that falls in the pass band of filter $H_0(f)$. The energy E_{21} is the energy in the first 512 samples in the passband of $H_1(f)$, and so on.

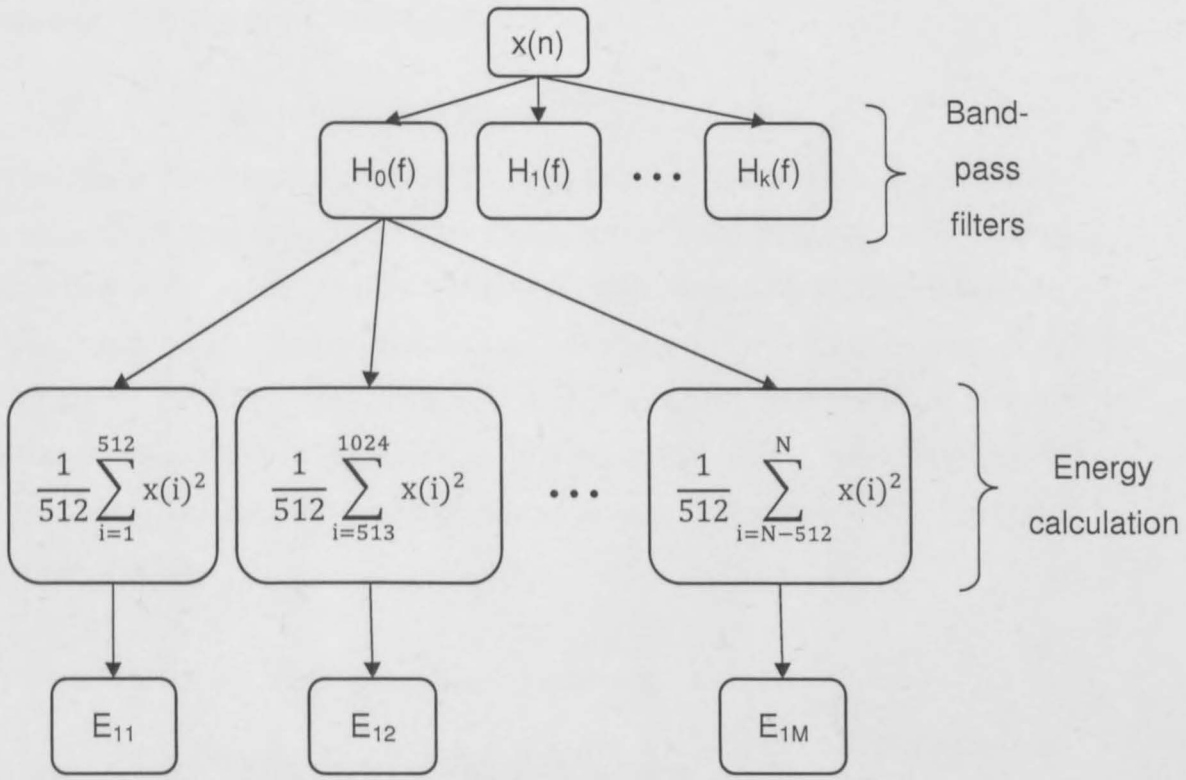

Figure 4.7. The Filterbank arrangement used in this study to calculate the energy per frame (512 consecutive samples of the time series).

The energy of each frame constitutes one observation of the signal x(n), being proceed:

$$\mathbf{X} = \begin{bmatrix} E_{11} & E_{21} & E_{31} & \cdots & E_{M1} \\ E_{12} & E_{22} & \vdots & & \vdots \\ E_{13} & \vdots & & & \\ \vdots & & & & \\ E_{1N} & E_{2N} & \cdots & & E_{MN} \end{bmatrix}$$

$$= \begin{bmatrix} \text{observation 1} \\ \text{observation 2} \\ \text{observation3} \\ \vdots \\ \text{observation N} \end{bmatrix} \qquad \text{Equation 4.7}$$

Here M is the number of filters in the filterbank, and consequently the number of subbands the signal is split into, and N is the number of consecutive frames into which the signal x(n) is divided.

4.3.3 Fisher discriminant analysis (FDA)

In the supervised learning context it is possible to use the class information, contained in target vector ***t***, to obtain an optimal mapping into a lower dimensional space to simplify the classification task and to gain insight into class separability. Fisher discriminant analysis (FDA) is a popular linear method for dimensionality reduction and it achieves this by minimizing the within-class scatter, a measure of the variance within each class, while maximizing the between-class distances so as to improve class separation (Fisher, 1936).

The within-class scatter matrix, $\mathbf{S}_w$, is expressed as:

$$\mathbf{S}_w = \sum_i p_i \mathbf{S}_{wi} \qquad \text{Equation 4.8}$$

with p_i the a priori probability of class w_i and $\mathbf{S}_{wi}$ the covariance matrix of class w_i. The covariance matrices are calculated as follows

$$\mathbf{S}_{wi} = \sum_{x \epsilon w_i} (\mathbf{x} - \boldsymbol{\mu}_i)(\mathbf{x} - \boldsymbol{\mu}_i)^T \qquad \text{Equation 4.9}$$

where ^{T} denotes the transpose and $\boldsymbol{\mu}_i$ is the mean vector of each class.

The between-class scatter matrix is defined as

$$\mathbf{S}_B = \sum p_i(\boldsymbol{\mu}_i - \boldsymbol{\mu}_a)(\boldsymbol{\mu}_i - \boldsymbol{\mu}_a)^T \quad \text{Equation 4.10}$$

with $\boldsymbol{\mu}_a$ the mean vector of all pooled classes given by

$$\boldsymbol{\mu}_a = \sum_i p_i \boldsymbol{\mu}_i \quad \text{Equation 4.11}$$

The within-class and between-class scatter matrices are transformed by projecting them to a lower dimensional space using a transformation matrix, **W**:

$$\tilde{\mathbf{S}}_B = \mathbf{W}^T \mathbf{S}_B \mathbf{W} \quad \text{Equation 4.12}$$

$$\tilde{\mathbf{S}}_W = \mathbf{W}^T \mathbf{S}_W \mathbf{W} \quad \text{Equation 4.13}$$

The optimal projection is that which maximises the between-class scatter and that minimizes the within-class scatter. Figure 4.8 illustrates the lower dimensional space which ensures optimal feature separation.

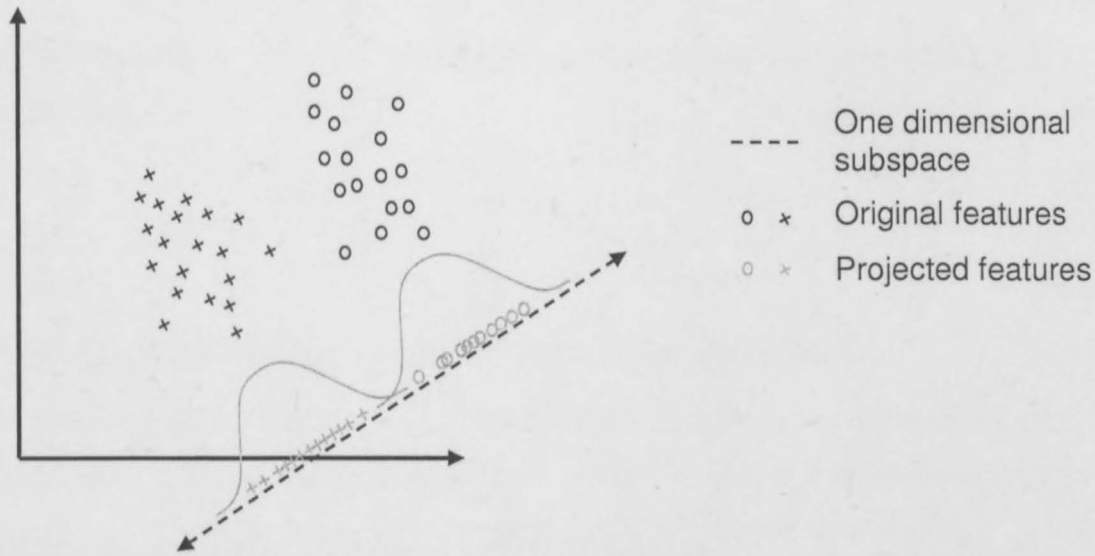

Figure 4.8. An illustration of the projection performed in Fisher discriminant analysis. on a two class problem (circles and crosses). The features are projected from a 2 dimensional space to the one dimensional subspace which ensure optimal linear data separation.

A scalar measure of scatter is the determinant of a scatter matrix, since the determinant is the product of the eigenvalues and hence the variance in the principal directions. From equations 4.12 and 4.13, and using the determinant measure we obtain the criterion function that defines the objective of FDA:

$$J(\mathbf{W}) = \frac{|\hat{S}_B|}{|\hat{S}_w|} = \frac{|\mathbf{W}^T S_B \mathbf{W}|}{|\mathbf{W}^T S_w \mathbf{W}|} \qquad \text{Equation 4.14}$$

It is interesting to note that by defining the total scatter as $\mathbf{S_T} = \mathbf{S_w} + \mathbf{S_B}$ then equation 4.14 can be written as

$$J(\mathbf{W}) = \frac{|\mathbf{W}^T S_T \mathbf{W}|}{|\mathbf{W}^T S_w \mathbf{W}|} - 1 \qquad \text{Equation 4.15}$$

Maximizing $\mathbf{J(W)}$ in equation 4.14 can be interpreted as maximizing the total scatter of the data (all classes) whilst minimizing the within class scatter.

The columns of the optimal transformation matrix, the $\mathbf{W}$ that maximizes $\mathbf{J(W)}$, are the eigenvectors that correspond to the largest eigenvalues in

$$\mathbf{S}_b \mathbf{w}_k = \lambda_k \mathbf{S}_w \mathbf{w}_k \qquad \text{Equation 4.16}$$

where $\mathbf{w}_k$ and λ_k are the corresponding eigenvectors and eigenvalues to be evaluated.

4.3.4 Kernel based Fisher discriminant analysis (KFD)

For real - world problems, linear methods are not always sufficient (Bo et al., 2006) and in the following chapter it will be shown that this is the case with the project at hand, at least with regards to Fisher discriminant analysis. This leads us to nonlinear methods, more specifically kernel methods, to exploit the nonlinear features in the data to be analyzed. The kernel based Fisher discriminant (KFD) method was first presented in the thesis of Sebastian Mika (2002) and a detailed derivation thereof will not be presented in this document. However, an overview of how kernel methods work is presented

here as motivation for the use of the KFD method to extract features from the data.

The basic idea of kernel methods is to employ a nonlinear mapping function, Φ, to map data from the input space, X, to a higher dimensional (possibly infinite dimensional) feature space, $\mathcal{E}$, where the data are then processed using popular linear algorithms. The mapping can be expressed as

$$\Phi: X \rightarrow \mathcal{E} \qquad \text{Equation 4.17}$$

$$\mathbf{x} \mapsto \Phi(\mathbf{x}) \qquad \text{Equation 4.18}$$

Where X is the input space and $\mathcal{E}$ is the new feature space, $\mathbf{x}$ a feature in the input space and $\Phi(\mathbf{x})$ the feature mapped to the feature space.

In effect, the nonlinear mapping provides access to nonlinear information in the data using relatively uncomplicated linear functions. See Figure 4.9 for an illustration of the effect of the nonlinear mapping.

In certain cases there might be enough information a priori to design the appropriate mapping function. If this mapping is not too complex to work out and $\mathcal{E}$ not too high in dimensionality, the data can be mapped and processed directly in the feature space (Mika, 2002).

However, the strength of kernel-methods lies in that the mapping function does not have to be calculated or even known in order to evaluate algorithms in the feature space. This is known as the *kernel trick*. As long as the original algorithm (in this study the linear algorithm is FDA) can be formulated such that its evaluation requires only scalar dot products a *kernel function* can be employed to evaluate the algorithm in the huge feature space (Mika, 2002).

If we consider the mapping expressed by equations 4.17 and 4.18; given two points $x_i \in X$ and $x_j \in X$, the function that returns the dot product of their

images in the feature space $\mathcal{E}$ is known as the *kernel function* (Lanckriet et al., 2004).

Definition: *A kernel is a function k, such that* $k(x,z) = \langle \Phi(x), \Phi(z) \rangle$ *for all* $x, z \in X$, *where* Φ *is the mapping from input space X to a feature space (also referred to as the dot product space)* $\mathcal{E}$. *A kernel matrix is a square matrix K* $\in \mathbb{R}^{n \times n}$ *such that* $K_{ij}=k(x_i, x_j)$ *for some* $x_1,\ldots,x_n \in X$ *and some kernel function k.*

The kernel matrix is positive definite that is to say it satisfies

$$\sum_{ij=1}^{n} r_i r_j K_{ij} \geq 0 \qquad \text{Equation 4.19}$$

for all $r_i \in \mathbb{R}$ and since it specifies the inner product. In both the State Space - Kernel Fisher Discriminant Analysis (SS-KFD) method and Filterbank – KFD (FB-KFD), used in this study, a Gaussian radial basis function (RBF) is used as the kernel function, which is expressed as

$$k(x,z) = e^{\frac{-\|x-z\|^2}{c}} \qquad \text{Equation 4.20}$$

Here c is the kernel function's hyperparameter, which is chosen by the user. In the case of the Gaussian RBF, c is the width of the kernel which is related to the variance of the normal distribution. By changing the hyperparameter, the basis functions of the feature space are changed. In this way the user can adjust the level of nonlinearity of the feature space. A smaller hyperparameter, with regards to the RBF kernel, translate to a narrower Gaussian basis function and hence increased nonlinearity. A larger hyperparameter translates to a wider or flatter and hence more linear Gaussian basis function.

To summarize, kernel methods work by mapping data into a nonlinear space, called the feature space, in which linear techniques (FDA) may perform better at separating the data, see Figure 4.9.

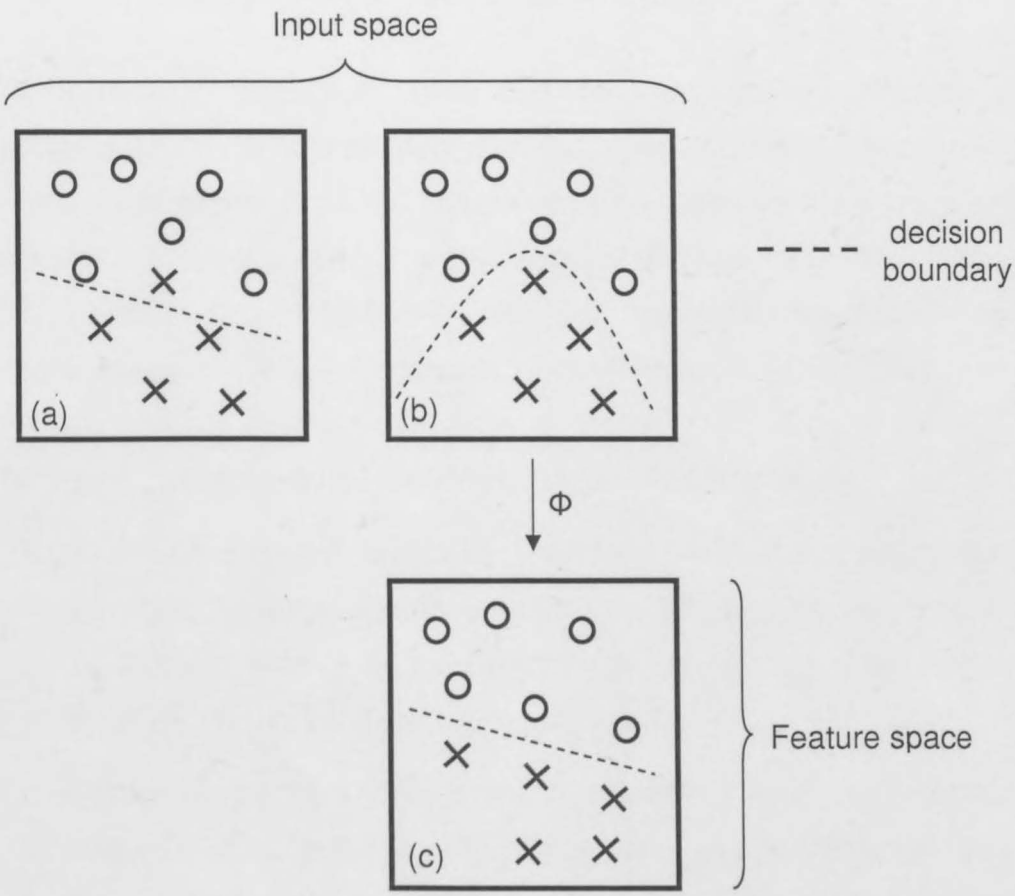

Figure 4.9. The cirlces and crosses class separation problem presented here cannot be separated without error using a linear decision boundary in the input space, (a). Improved separation can be achieved in the input space using a nonlinear decision boundary, as illustrated in figure (b). This nonlinear decision boundary in the input space corresponds to a linear decision boundary in the feature space, shown in figure (c). Using an appropriately selected mapping function, Φ, which is implied by the kernel function *k*, the data points are mapped from the input space to the feature space where they are processed using linear techniques.

The mapping is performed implicitly by specifying the dot products between each pair of points in the feature space. This information is contained in the kernel matrix *K*, a n by n symmetric, positive definite matrix, where n is the number of data points. In this study an RBF kernel is used as a nonlinear mapping function, Φ, and the linear technique used to separate the data in the feature space for classification is FDA.

4.4 K nearest neighbour classification

The k nearest neighbour (kNN) classifier was chosen because of its tractability and ease of implementation. However, since no processing is done before classification, the kNN classifier can be costly from a storage point of view and can suffer greatly under the curse of dimensionality. That is to say, a kNN classifier's computational complexity worsens significantly as the dimensionality of the train features increase (Theodoris et al., 2004).

The algorithm employed by the kNN classifier is as follows:

- Given an unknown (test) feature vector **x**, the *k* closest train vectors are identified. As suggested by (Marques de Sá, 2001) *k* should be chosen as odd and should not be a multiple of the number of classes so that there will always be a unique classification.
- Assign the vector **x** to the class, w_i, to which most of the *k* nearest train vectors belong. In the classification experiments performed in this study, the Euclidean distance measure was used to determine the distances between a test feature and the train features that comprise the kNN model.

Figure 4.10 illustrates the KNN decision with respects to a two class classification.

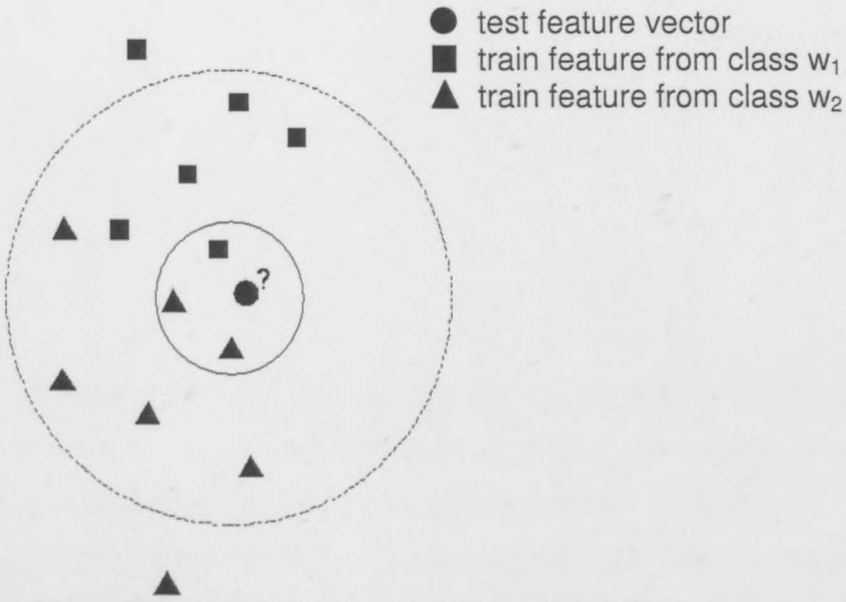

Figure 4.10. The KNN classifiers decision rule for a two class classification.

If *k* is chosen to be 3, in Figure 4.10 above, it is clear that the unknown feature vector (the blue circle in Figure 4.10) will be assigned to class w_2 (represented by the red triangles).

4.5 Summary

In this chapter the pattern recognition methodology which was followed in this study, of which an overview is presented in Figure 4.1, was discussed. Some results were presented in Section 4.2.2 regarding the removal of outliers from the acoustic signals in the database. The outlier removal process involved extracting outlier free portions from the acoustic signals. Due to the amount of outliers present in the most corrupt acoustic signal, the longest portion which could be extracted from this signal was 10 000 samples in length. All the acoustic signals were therefore evaluated using an outlier removal process which extracted 10 000 outlier free portions from them.

Chapter 5

Results

5.1 Introduction

The portion of the database that was used to obtain the results discussed in this chapter, consists of the five experimental runs that were made at a low current setting and that included all arc lengths from 5 to 30 mm (see Table 1). It was decided that 5mm increments (in arc length) are not representative to the incremental settings in use within the industry. The data were therefore split into 2 separate sets, each containing recordings made with 1 cm increments. Hence data set one contained the recordings made at 5, 15 and 25 mm arc lengths, whereas data set 2 contained those made at 10, 15 and 30 mm. Also, for reasons relating to outlier removal and discussed in section 4.2.2, the useable data were limited to approximately 10 000 consecutive outlier free samples per recording. See Figure 5.1 for a layout of the data used to obtain the results presented in this chapter.

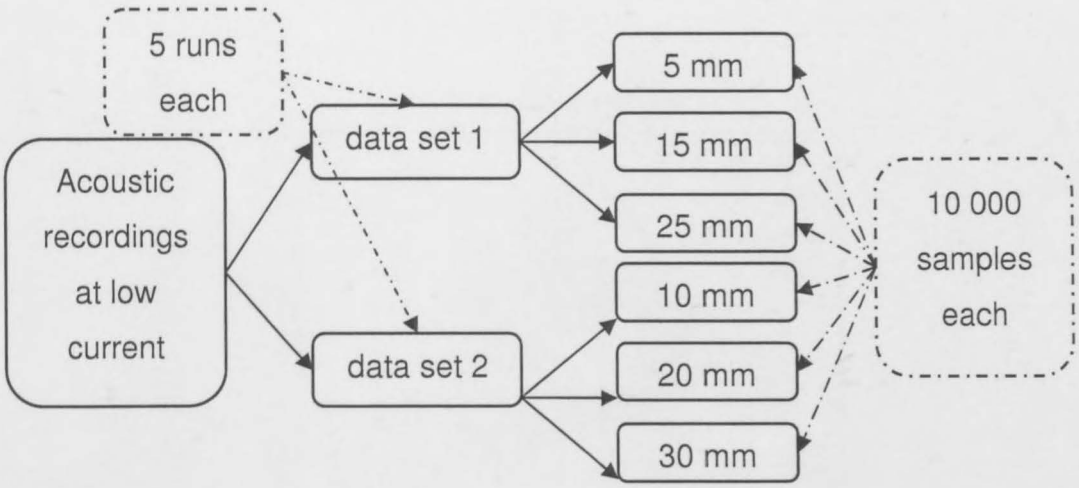

Figure 5.1. The data sets used for feature extraction and classification.

The models in this chapter were trained and tested using two different approaches. In the first, features were extracted from data obtained during a single experimental run and then randomly split into 60% train features and 40% test features. In the second method all the data from a single or multiple experimental runs were used to obtain train features and the remaining experimental runs were then used to obtain test features.

5.2 State Space Kernel Fisher Discriminant Analysis (SS-KFD)

The SS-KFD method was only considered when it became clear that the linear Fisher discriminant analysis (FDA), was not providing adequate data separation. This is illustrated in Figure 5.2 that presents the state space features before (top) and after (bottom) FDA.

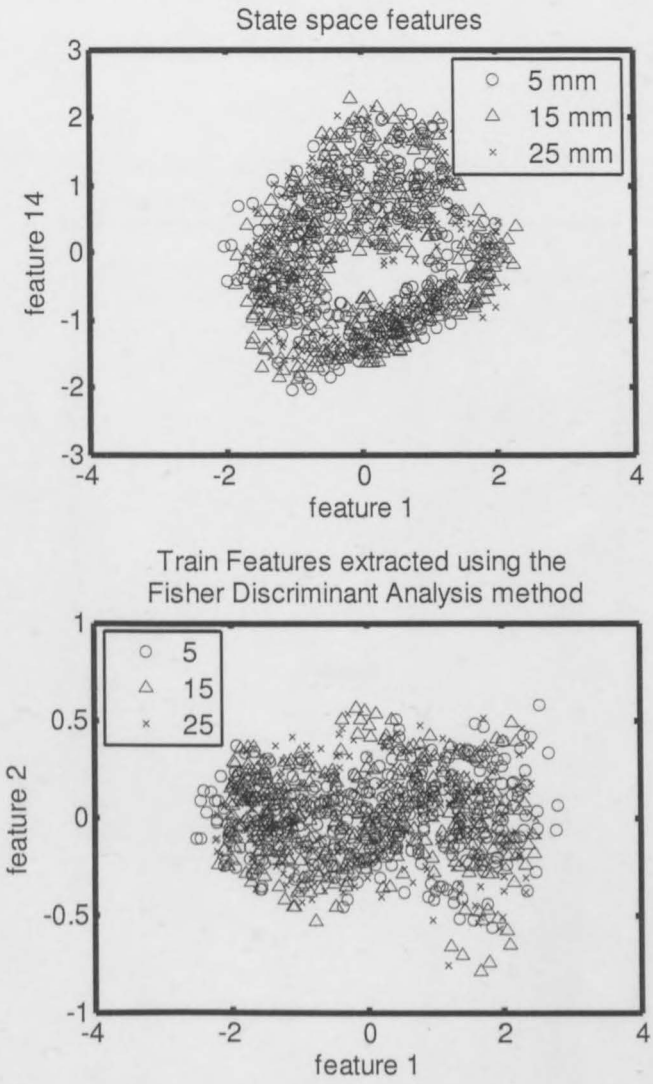

Figure 5.2. State space features before (top) and after (bottom) Fisher discriminant analysis.

We recall from Chapter 4.3.3 that the FDA method projects the state space features onto a set of orthogonal linear basis functions that maximize the between-class separation and minimize the within-class separation. As can be seen in Figure 5.2 (bottom), whilst the within - class separation is reduced, hardly any between - class separation is achieved using FDA method.

This led to the exploration of nonlinear methods (kernel methods) and Figure 5.3 presents the features obtained using the same state space features, as in Figure 5.2., but applying the SS-KFD method with a hyperparameter, c, of 0.1.

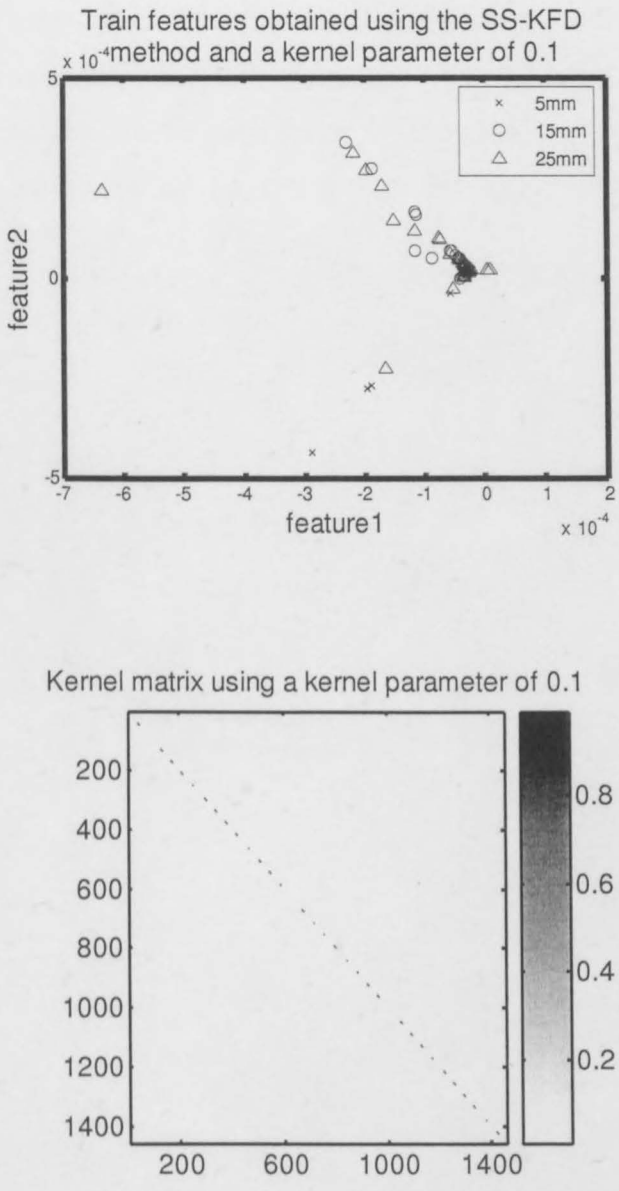

Figure 5.3. An illustration of over fitted train features (above) obtained using SS-KFD method with a kernel parameter of c = 0.1, together with the corresponding kernel matrix (below).

As can be seen from the above features, the data separation is slightly improved, however, the kernel matrix contains no structure in its off diagonal

elements, indicative of a poorly learned KFD model (we recall from the definition presented in Chapter 4.3.4, that the kernel matrix can be viewed as a map of the evaluation of the linear algorithm in the feature space). Intuitively a larger hyperparameter is used since the sharpness in the positioning of the features as well as the lack of structure in the kernel matrix is indicative of a RBF kernel with to narrow a width (the smaller c is chosen, the narrower and hence less linear the basis functions of the feature space). Figure 5.4 presents the features extracted using the SS-KFD method with a hyper parameter of 1.

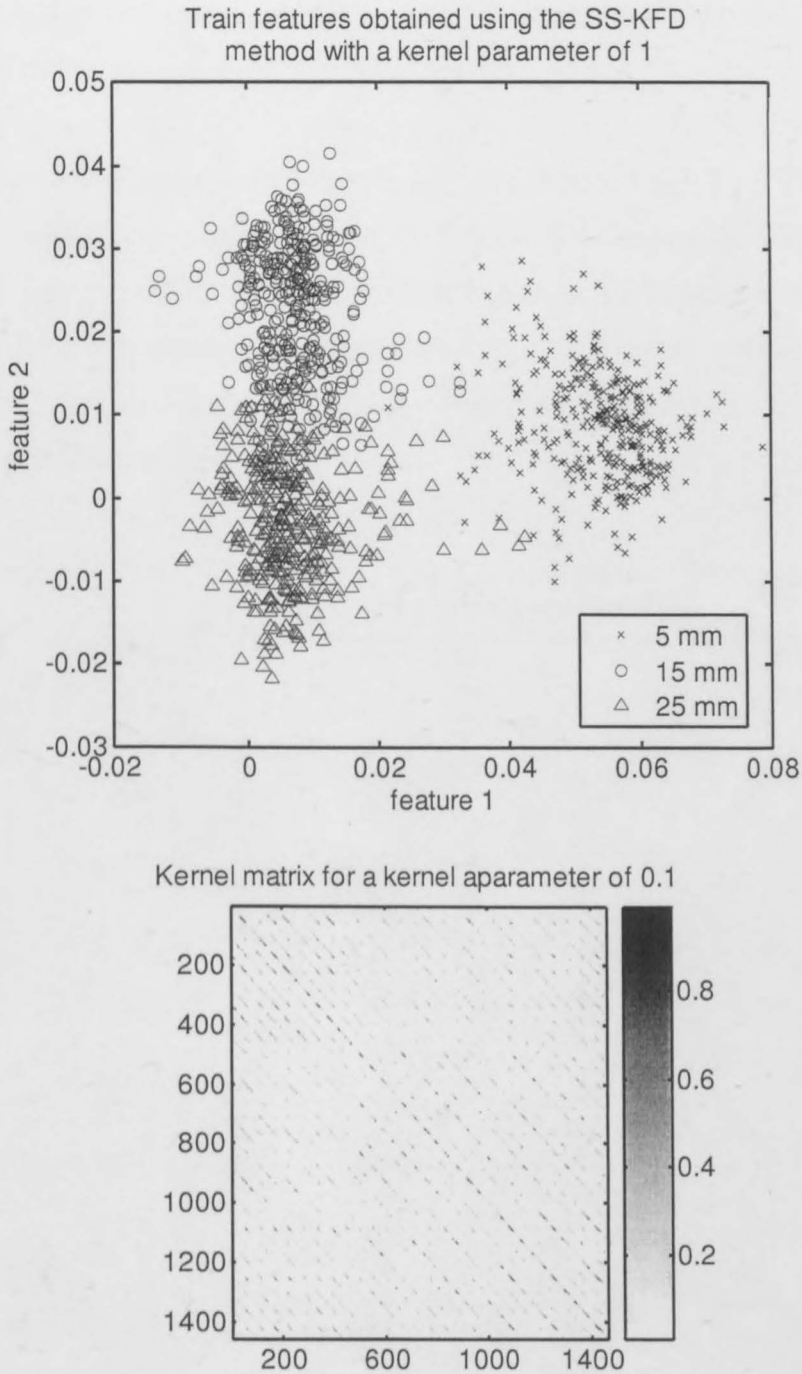

Figure 5.4. An illustration of train features (above) obtained using SS-KFD method with a kernel parameter of 1, together with the corresponding kernel matrix (below).

The features presented in Figure 5.4 show that improved data separation is obtained using a larger and hence "smoother" kernel parameter. For the RBF

kernel, a larger hyperparameter translates to a broader kernel. The kernel matrix shows some structure in the off-diagonal elements indicative of improved learning.

Figure 5.5 below presents the test features extracted with the SS-KFD model used to obtain the train features in Figure 5.4 and a decision boundary obtained using a kNN classifier with k equal to 5. These test features we obtained from the same experimental run data as the train features presented in Figure 5.3 and Figure 5.4 above. The results obtained from this model showed a 9.5% prediction error.

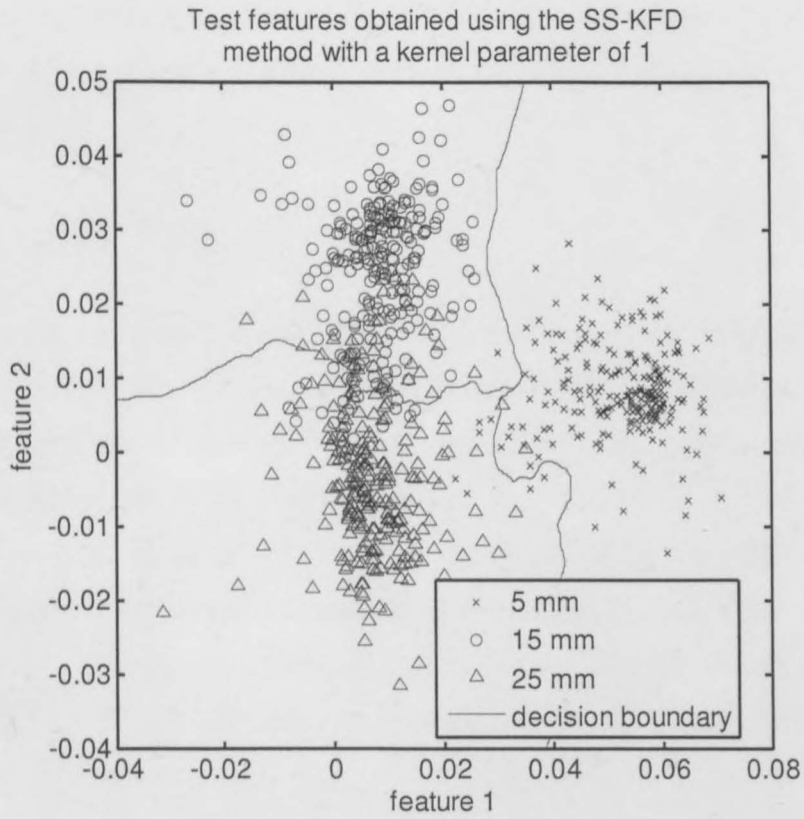

Figure 5.5. An illustration of test features (above) obtained using SS-KFD method with a kernel parameter of 1, together with the corresponding decision boundary as obtained using a 5 nearest neighbour classifier.

Even though good classification accuracy was obtained using this method, the question that still needed to be answered is how well the SS-KFD method would perform on unknown data. This is an important part of a classifiers' design that is known as the generalized performance of the classifier.

To test the generalized performance of the KFD features, the data sets were reorganized to train models using certain runs and tested using the remaining runs. For instance a model was trained on run 1 and tested using runs 2, 3, 4 and 5 alternately. Also, training was performed using 2 runs or more and testing on the remaining ones.

This method requires a significant number of trained models. For instance the number of different combinations (without repetition) of 2 runs that can be drawn from 5 is

$$\binom{5}{2} = \frac{5!}{2!(5-2)!} = 10 \qquad \text{Equation 5.1}$$

Testing on the remaining 3 runs for each combination translates to 30 train and test combinations while training a single model takes approximately 2 hours. The computational complexity of the SS-KFD method is dominated by the formulation of the N by N kernel matrix (as described in Chapter 4.3.4), where N is the number of training samples. Due to this very high computational complexity, I moved onto classification experiments using a kernel based filterbank approach, since due to the filterbank's data compression attributes, a filterbank method promised to be computationally less taxing.

5.3 The Filterbank - Kernel Fisher Discriminant Analysis (FB-KFD) Method

5.3.1 Filterbank Design

To construct the filterbank, a prototype filter was designed from which all filters in the filterbank was derived. Figure 5.6 illustrates the difference in the frequency responses between two most popular filter types, namely the Butterworth filter and the Chebychev filter.

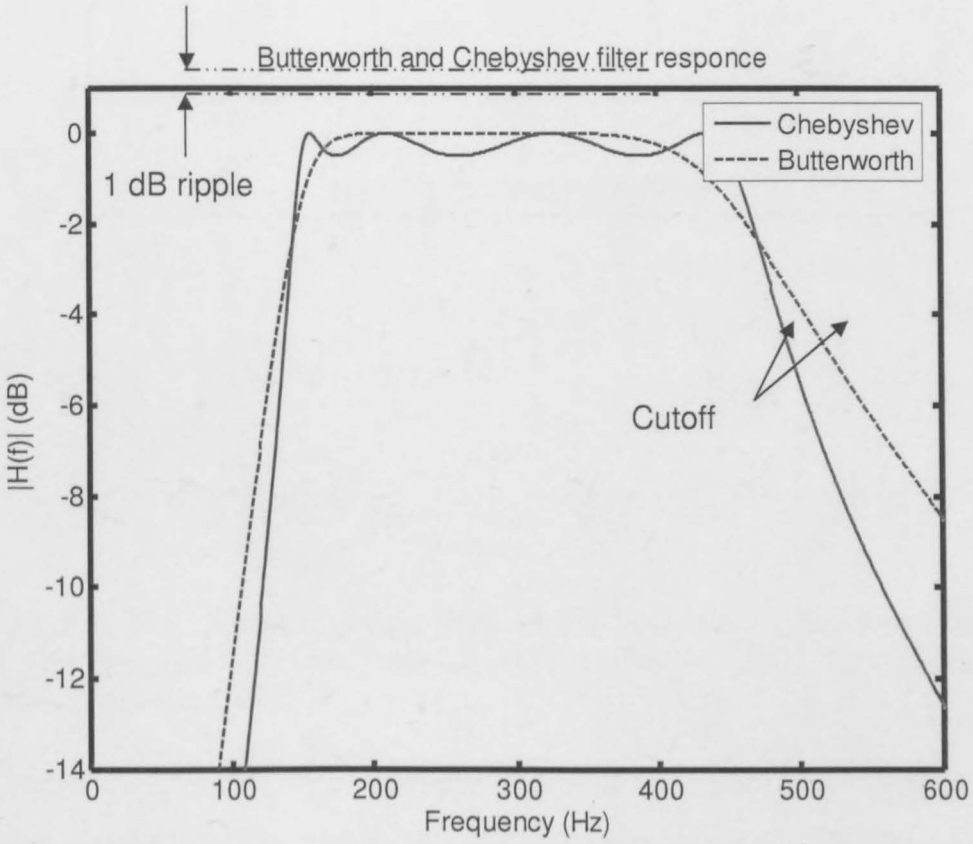

Figure 5.6. An illustration of the differences between Butterworth and Chebyshev bandpass filters, with pass bands of 150 to 450 Hz.

The Butterworth filter was chosen for its low pass band ripple and since the slow cutoff is of no consequence. The filterbank uses overlapping filters to ensure that no information was lost through filtering. Figure 5.7 illustrates the final filterbank design as well as the frequency response of the prototype filter.

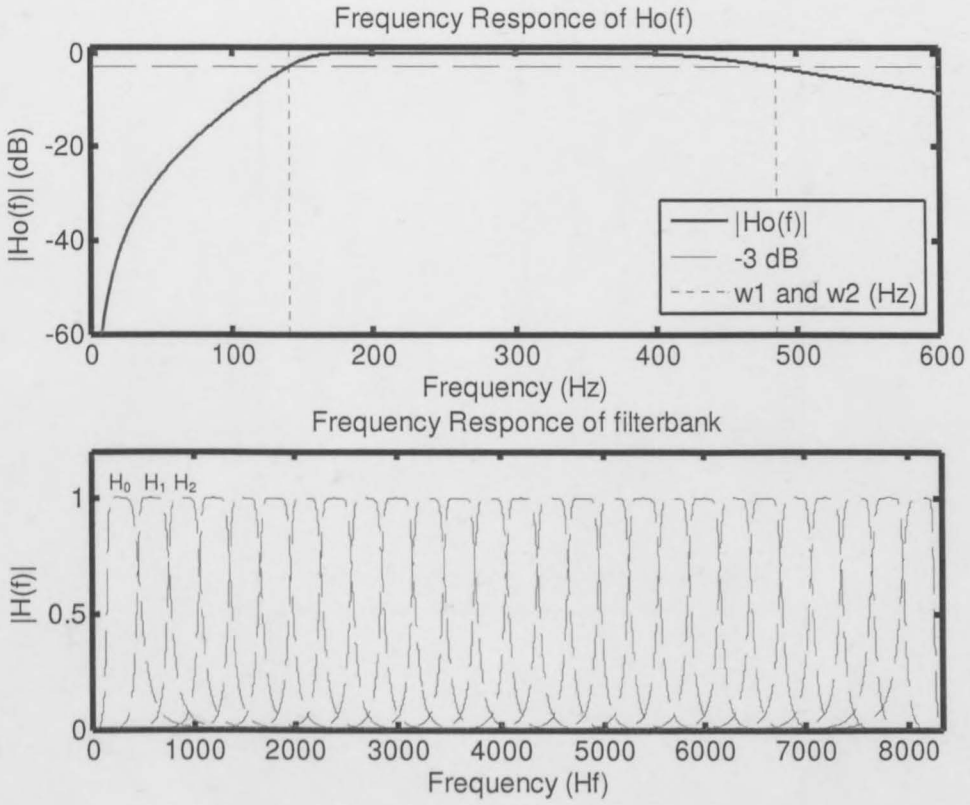

Figure 5.7. The frequency response of the first band pass filter (above) and the parallel combination of filters (below) that constitute the filterbank arrangement.

We recall from Section 4.3.2 that the output of the band pass filters must be divided into frames. The energy per frame, as passed by the band pass filters, constitutes the features obtained from the filterbank. Care was taken not to choose a frame width which would be to so small and as a result low frequency information would be lost. However, the smaller the frame width the more frames and hence more features can be obtained from the acoustic signal.

The lowest frequency component in a typical acoustic signal from the database can be obtained by inspecting the signal's frequency spectrum, presented in Figure 5.8.

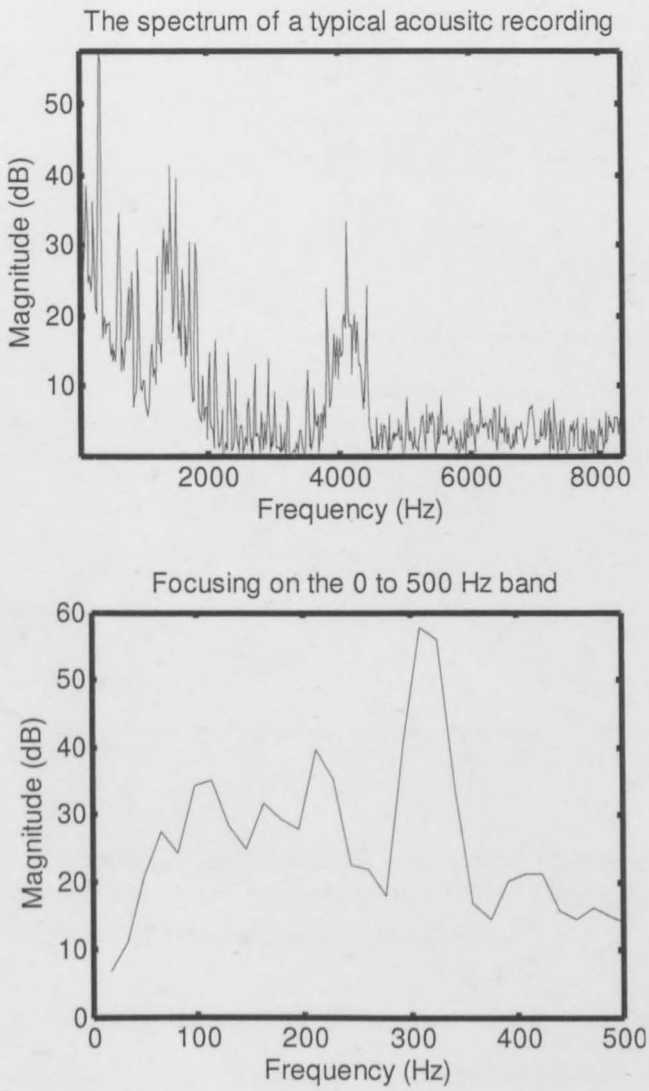

Figure 5.8. The frequency spectrum of a typical acoustic recording (above) and focusing in on the 0 to 500 Hz frequency band (below).

It is clear that the lowest frequency component is approximately 50 Hz. At 16 667 samples per second (the sampling frequency used during data acquisition), one period of a 50 Hz sinusoid is 333 samples long. The frame width should thus exceed this and be a power of 2 for the efficient calculation of the fast Fourier transform (FFT, a popular algorithm used in many spectrum analysis methods). Consequently a frame width of 512 was chose. Figure 5.9 illustrates the difference in filterbank energies when using different frame widths.

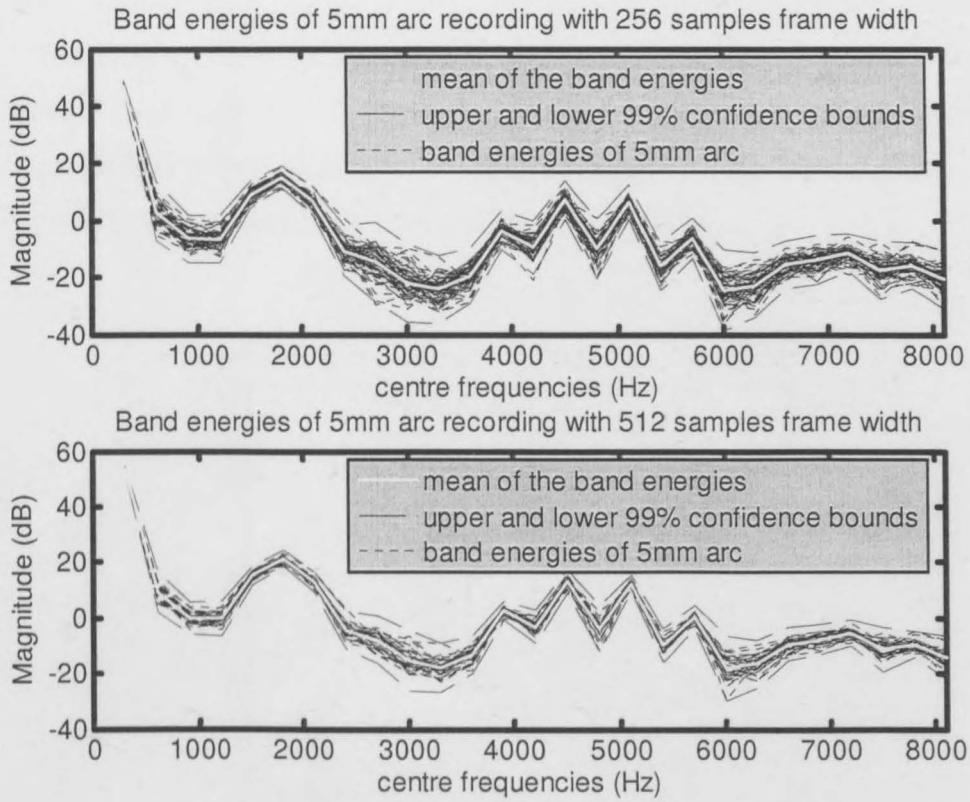

Figure 5.9. The filterbank energies of a recording taken at an arc length of 5mm with a prototype filter bandwidth of 300 Hz and frame width of 256 (top) and 512 (bottom) samples respectively.

We can see that the variance of the filterbank energy, as portrayed by the width of the confidence bounds, increases with a decrease in frame width.

5.3.2 Single run results

Before testing the generalized performance of the FB-KFD method, results were obtained using a single run for both training and testing. This was done to determine the ideal hyperparameter value and to investigate the single - run performance of the method. A bootstrap method was employed here to increase confidence when using a small data set. The term bootstrapping here refers to the technique employed when working with a small labelled data set (the data from a single experimental run) to induce a classifier and estimate its performance with reference to a larger set of unlabelled or unknown data (Abney, 2002).

The method adjusts the hyperparameter as indicated in Figure 5.10 and randomly subsamples train and test data with replacement from a single run. FB-KFD models are then trained using the various hyperparameter values and randomized train data. The prediction error is determined and the process is repeated ten times. Figure 5.10 presents the results obtained from this tenfold prediction method using a boxplot.

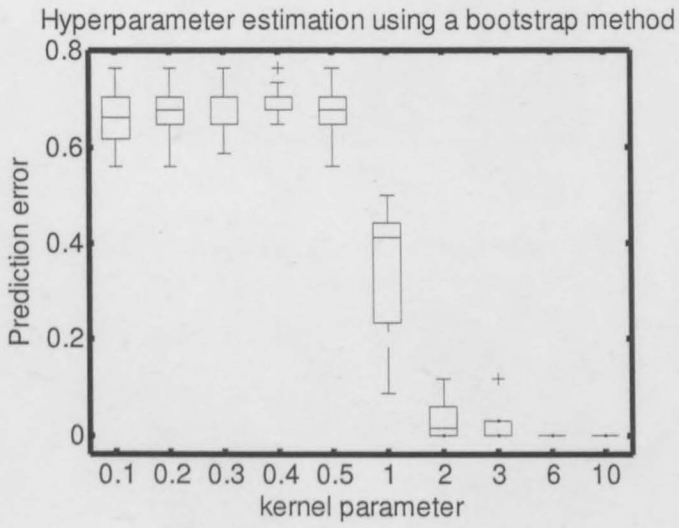

Figure 5.10. Hyperparameter estimation using a bootstrap method.

The boxplot indicates that a larger hyperparameter is favourable. Figure 5.11 illustrates the kernel matrix obtained using the FB-KFD method and hyperparameters values of 10 and 50.

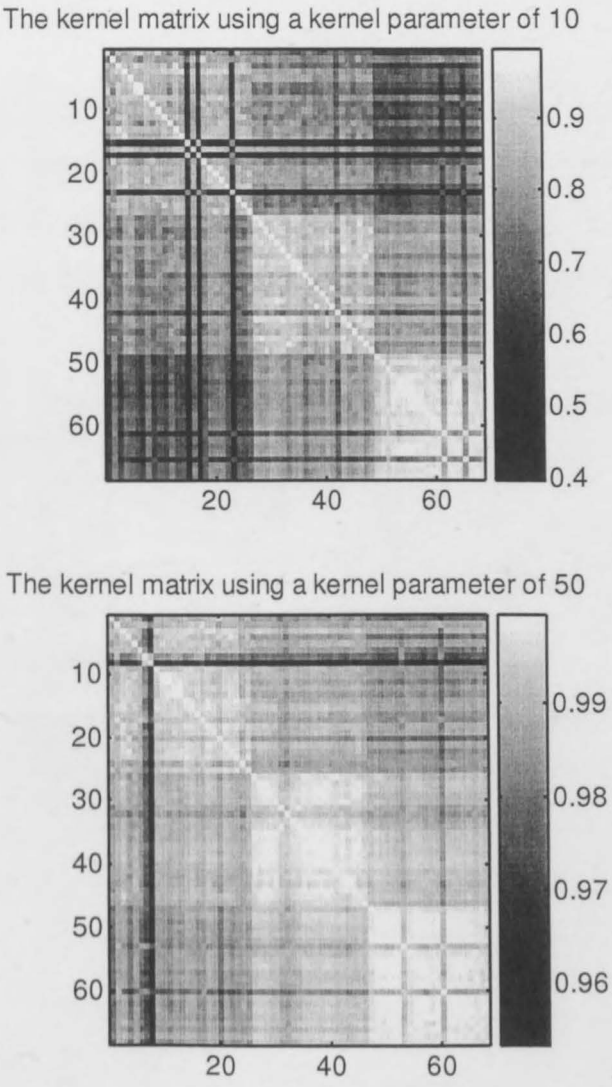

Figure 5.11. The kernel matrix obtained using the FB-KFD method with a hyperparameters of 10 (above) and 50 (below).

Even though both the 10 and 50 hyperparameter kernel matrices show structure in their off diagonal elements, when compared to the those obtained in Section 5.2, the kernel matrix with a hyperparameter of 10 has a range that covers 0.4 to 1 whilst the kernel matrix with a hyperparameter of 50 only covers 0.96 to 1. An increase in range is indicative of improved learning and hence motivates the choice for a hyperparameter that is not 'too large.'

Consequently a hyperparameter of 10 was selected to train all subsequent models.

In Figure 5.12, two figures are presented that illustrates how improved data separation is obtained when using the FB-KFD method as opposed to just the FB method. The filterbank features (above left and right) are a visual representation of the 27 features obtained from the filterbank.

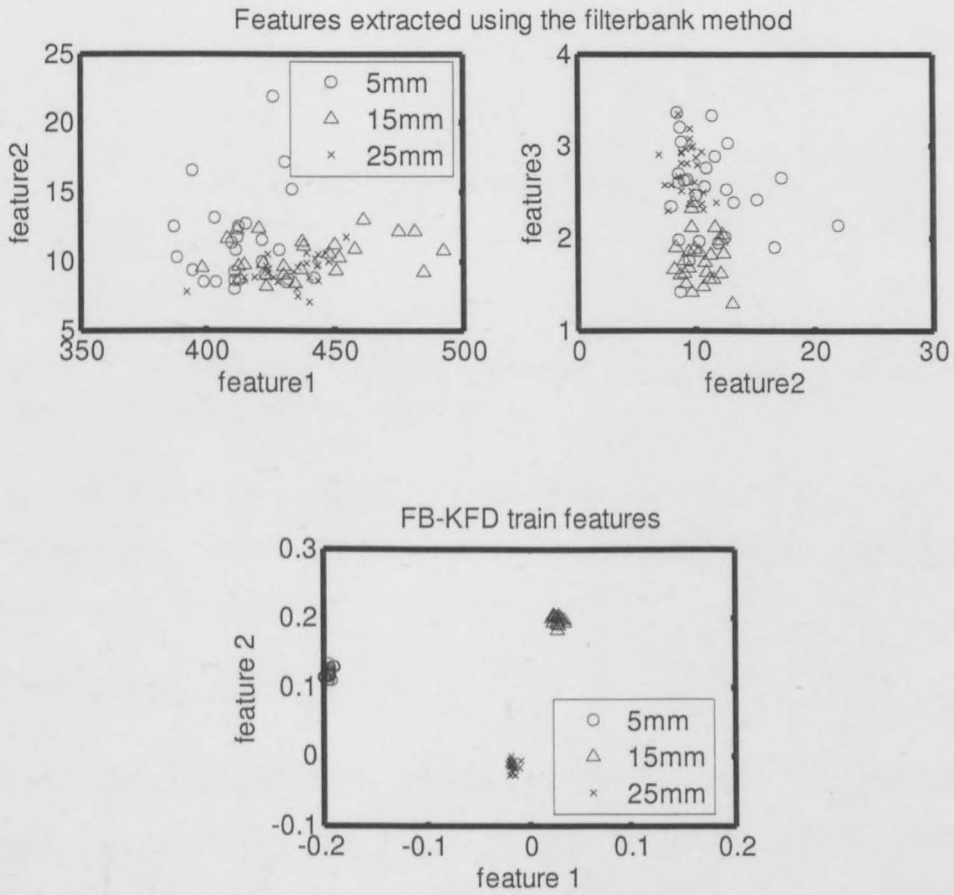

Figure 5.12. The Filterbank (FB) features before (above and middle) and after (below) kernel based fisher discriminant analysis (KFD) is performed.

In Figure 5.13 the corresponding test features are displayed together with the decision boundary obtained using a 5 nearest neighbour classifier and the

train features above. Again an improvement in comparison to the SS-KFD method is evident, see Figure 5.5.

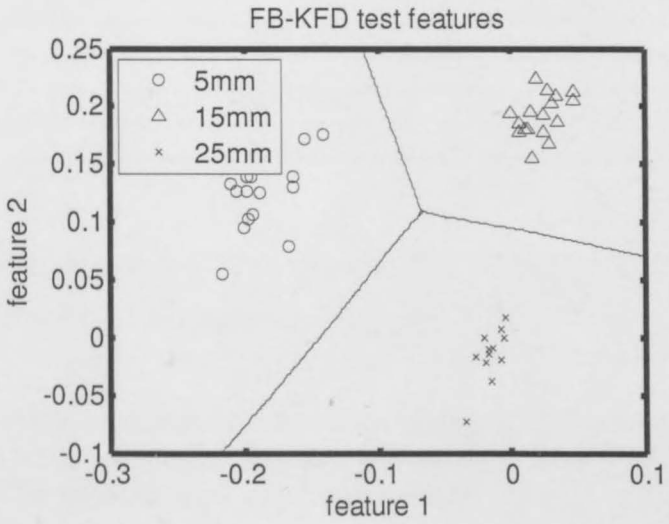

Figure 5.13. FB-KFD test features obtained using a model trained on the train features presented in Figure 5.12.

The prediction error obtained using a bootstrap method and data from a single experimental run to train and test with, is consistently 0% as expected when considering the results displayed in Figure 5.10.

5.3.3 Generalized results

The generalized results were obtained for the two data sets, described in Chapter 5.1, by evaluating KFD filterbank (KFD-FB) models using data collected from different experimental runs to train and test on. The method used here was to train models using all combinations of single to four run data and to test the models using a 5 nearest neighbour classifier and the data from the remaining runs/run. See Table 2 for a layout of the number of runs used to test and train the KFD-FB models with (column 1), as well as the number of combinations that is possible using the specified number of train runs (column 2) and the figures illustrating the results obtained.

Table 2. A summary of the combinations of runs used in obtaining the generalized performance of the KFD-FB method.

Number of train runs	Number of combinations without repetition	Number of individual test runs	Figure
1	5	4	Table 3
2	10	3	Table 4
3	10	2	Table 5
4	5	1	Table 6

Table 3 to Table 6 present the results that investigate the generalized performance of the FB-KFD method.

Table 3. The prediction errors obtained using KFD models trained with data obtained from a single experimental run, and tested using data obtained from the remaining experimental runs.

Data set 1

Train Run	Test Run				
	1	2	3	4	5
1		0.781	0.667	0.667	0.667
2	0.96		0.8421	0.719	0.746
3	0.667	0.482		0.518	0.64
4	0.675	0.474	0.412		0.333
5	0.667	0.395	0.649	0.43	

Data set 2

Train Run	Test Run				
	1	2	3	4	5
1		0.667	0.667	0.667	0.667
2	0.588		0.667	0.667	0.667
3	0.667	0.439		0.333	0.404
4	0.667	0.649	0.561		0.0702
5	0.64	0.667	0.5	0.667	

Table 4. The prediction errors obtained using KFD models trained with data obtained from two experimental runs, a hyperparameter of 10 and tested using data obtained from the remaining experimental runs.

Data set 1

Train Runs	Test Runs				
	1	2	3	4	5
1,2			0.658	0.667	0.561
2,3	0.623			0.483	0.404
2,4	0.554		0.246		0.325
2,5	0.447		0.64	0.272	
1,3		0.667		0.518	0.456
3,4	0.667	0.632			0.377
3,5	0.667	0.535		0.105	
1,4		0.763	0.36		0.342
4,5	0.667	0.605	0.36		
1,5		0.614	0.456	0.201	

Data set 2

Train Runs	Test Runs				
	1	2	3	4	5
1,2			0.667	0.667	0.71
2,3	0.667			0.561	0.228
2,4	0.482		0.351		0.0965
2,5	0.614		0.465	0.649	
1,3		0.667		0.658	0.579
3,4	0.667	0.333			0.097
3,5	0.579	0.658		0.5	
1,4		0.667	0.246		0.035
4,5	0.333	0.439	0.351		
1,5		0.667	0.386	0.553	

Table 5. The prediction errors obtained using KFD models trained with data obtained from three experimental runs, a hyperparameter of 10 and tested using data obtained from the remaining experimental runs.

Data set 1

Train Runs	Test Runs				
	1	2	3	4	5
3,4,5	0.544	0.64			
1,4,5		0.667	0.316		
1,3,5		0.667		0.237	
1,3,4		0.833			0.518
2,4,5	0.491		0.333		
1,2,5			0.386	0.123	
1,2,4			0.465		0.342
2,3,5	0.623			0.316	
1,2,3				0.412	0.403
2,3,4	0.465				0.184

Data set 2

Train Runs	Test Runs				
	1	2	3	4	5
3,4,5	0.544	0.412			
1,4,5		0.667	0.3161		
1,3,5		0.667		0.342	
1,3,4		0.667			0.123
2,4,5	0.64		0.325		
1,2,5			0.386	0.447	
1,2,4			0.325		0.132
2,3,5	0.658			0.439	
1,2,3				0.552	0.465
2,3,4	0.588				0.088

Table 6. The prediction errors obtained using KFD models trained with data obtained from four experimental runs, a hyperparameter of 10 and tested using data obtained from the remaining experimental runs.

Data set 1

Train Runs	Test Runs				
	1	2	3	4	5
2,3,4,5	0.509				
1,3,4,5		0.666			
1,2,4,5			0.404		
1,2,3,6				0.289	
1,2,3,4					0.281

Data set 2

Train Runs	Test Runs				
	1	2	3	4	5
2,3,4,5	0.632				
1,3,4,5		0.667			
1,2,4,5			0.377		
1,2,3,6				0.193	
1,2,3,4					0.254

These results are summarized in Figure 5.14. This figure illustrates the mean prediction error, upper and lower quantiles and the minimum and maximum prediction error that is obtained as the number of runs used to train a KFD-FB model is increased.

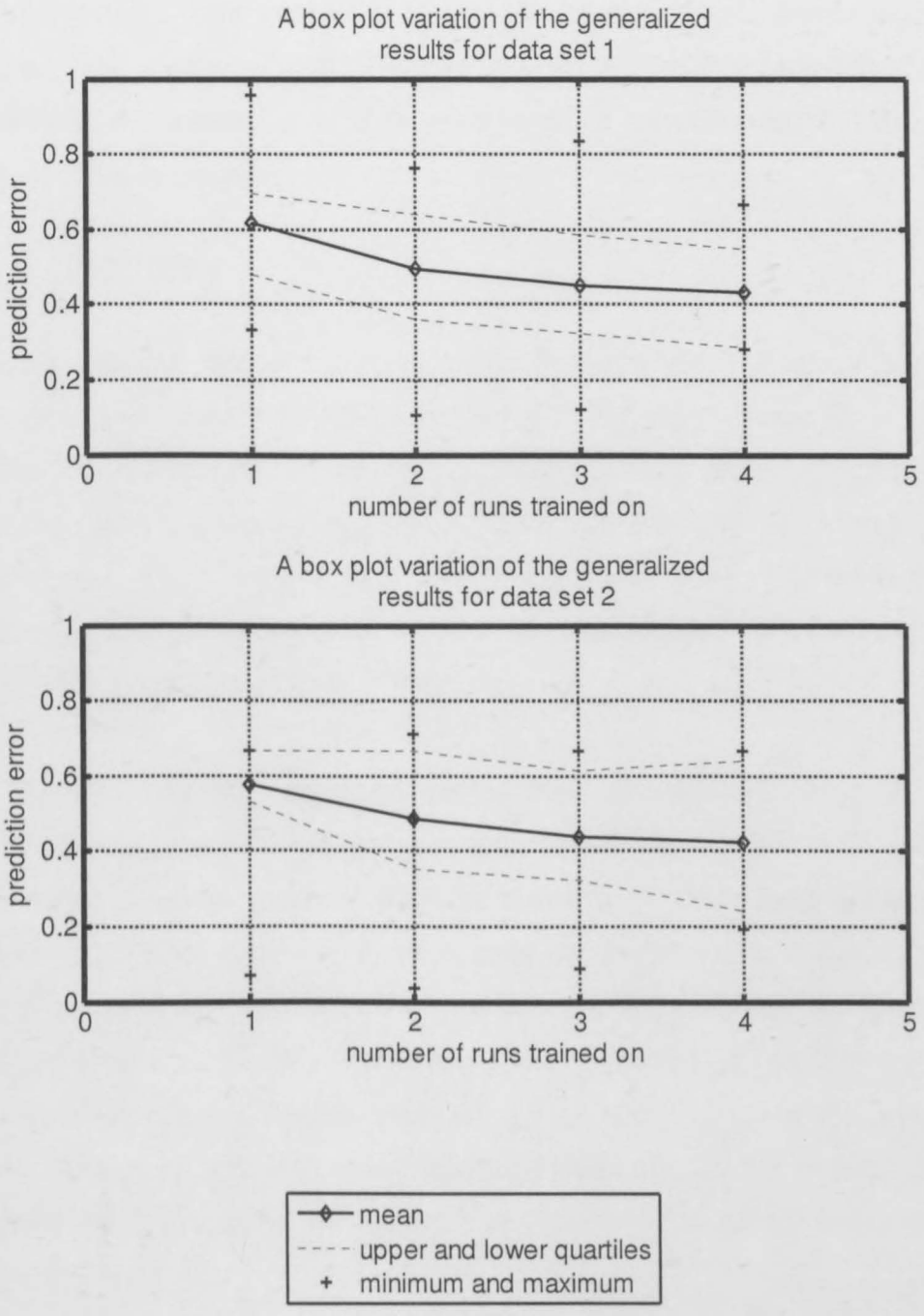

Figure 5.14. A variation on the box plot indicating the improvement in generalization as the number of runs used in training is increased. These KFD models were trained using a Kernel width of 10.

It is clear from Figure 5.14 that a trend exists which indicates that on average the more statistically representative the train data are, the better the KFD-FB

method performs on unknown data. While two experimental runs might have many parametric differences, (such as tolerances on the hand machined crucibles, the cathode which erodes constantly, and unavoidable small variations in the amount of charge used for each experimental run) five runs will have more in common.

5.4 Summary

In this chapter two methods used to extract features from the acoustic portion of the database, namely SS-KFD and FB-KFD analysis methods. Even though the SS-KFD method performed well, obtaining a 9.5% prediction error when evaluated using a 5 nearest neighbour (5NN) classifier and data from a single experimental run to extract train and test features from, the method was computationally too expensive to test its generalized performance. This motivated the use of the FB-KFD method.

The FB-KFD method performed better than the SS-KFD method when evaluated using data from a single experimental run as both train and test data. It consistently obtained prediction errors of 0%, using a bootstrap method and a 5NN classifier, these results are presented in Figure 5.10. To test the generalized performance of the FB-KFD method, train features were extracted from a single or multiple experimental runs and the 5NN classifier was trained with them. Test features were then obtained using the remaining experimental runs with which the classifier's performance was evaluated. The results of the generalized performance of the FB-KFD method are presented in Figure 5.14.

On average the classifier did not perform much better than chance (with three classes a chance prediction error is 67%) when trained with features obtained from a single experimental run. However, when using train features from four experimental runs, the mean prediction error obtained was 43%, noticeably better than chance with an improvement of approximately 20%. The best models obtained prediction errors below 20% indicating that good prediction is

possible in some cases. This may be attributed to increased likeness in conditions of the experiments from which the data is drawn to train and test these models.

Overall indications are that it is indeed possible to predict arc length from arc acoustics, and that with training data that is statistically representative of the unknown or test data a substantial improvement in classification accuracy can be expected. At present, however, it is regrettably not possible to compare these results with current industrial methodology of arc length control. This is due to the unavailability of literature that quantifies the inaccuracies in current methods. However, the inaccuracies have been acknowledged (Drouet and Nadeau, 1982) and it is therefore recommended that a future study should focus on quantifying them.

Chapter 6

Summary, Conclusions and Future Work

A database of acoustic, voltage and current signals produced by a dc electric arc furnace was collected. The database together with the equipment developed for data acquisition form part of the results of this project. During data acquisition, recordings were made at the three different current settings and at arc lengths of 5, 10, 15, 20, 25 and 30 mm. The largest portion of the database includes the recordings made at a low current setting and this portion of the database was consequently used for pattern recognition.

Two feature extraction methods were evaluated in a series of pattern recognition experiments, the first state space (SS) embedding and the second filterbank (FB) analysis. The initial attempt at finding linear decision boundaries using Fisher discriminant analysis (FDA) proved unsuccessful. The nonlinear kernel Fisher discriminant analysis (KFD) technique was then used to extract features from the state space (SS) and filterbank (FB) feature vectors in what would effectively have amounted to a double-stage feature extraction process. A k nearest neighbour (kNN) classifier, with k equal to 5, was used to evaluate the classification accuracy of these features.

As a first attempt, features from a *single experimental* run were used to train and test the classifier, using both the SS-KFD and FB-KFD features. The classifier obtained prediction errors of 9.5% using the SS-KFD features and 0% using the FB-KFD features, using a ten fold bootstrap method for integrity.

At this point it became clear that the SS-KFD method would be computationally too taxing and the FB-KFD method was considered for further assessment.

Although the different arc lengths could be identified perfectly in a single experimental run, this was not the case when data from multiple runs were considered, since the behaviour of the arc in the furnace varied markedly between experimental runs. Therefore, the generalized performance, that is to say the performance on unknown data, of the FB-KFD features was evaluated by training the classifier first with acoustic recordings made during a single experimental run and then with recordings made during multiple experimental runs.

The classification accuracy was evaluated using FB-KFD features obtained from the remaining experimental runs as test features. On average a classifier trained using four experimental runs had a mean prediction error of 43%, noticeably better than chance, where chance refers to a prediction error of 67%. The best models obtained prediction errors below 20%, indicating that good classification is indeed possible.

The generalized performance of the FB-KFD features exposed a trend which indicates that if training data that are statistically more representative of the test data are used, an improvement in the classifiers' performance can be achieved. This result not only suggests that there is a relationship between arc length and arc acoustics, but that this relationship can be exploited to develop a sensor for the detection of arc length from arc acoustics in the dc EAF.

Future work should include an investigation into the effect different current levels would have on the classification accuracy. Theoretically the classifier can be trained using features extracted from both the current and acoustic

signals, and its performance evaluated using the methods discussed in this thesis.

Finally, a study should also be performed to investigate how frequently arc instability occurs in practice, where the term arc instability refers to arc anomalies that differ from normal operating conditions. It is also not clear what effect such anomalies may have on the prediction of arc length from arc acoustics.

References

Abney, S. 2002, 'Bootstrapping', *The Proceedings of the40th Annual Meeting of the Association for Computational Linguistics*, pp 360–367, Philadelphia

Babcock, W.R., Baker, K.L., Cattaneo, A.G. 1968, *'Musical Flames'*, *The Journal of the Acoustical Society of America*, vol. 43, no. 3, pp 1465-1466

Barker, I. J. 1980, 'An Electrode Controller for Submerged Arc Furnaces', IFAC Mining, Mineral and Metal Processing, Canada

Bo, L., Wang, L., Jiao, L. 2006, 'Feature Scaling for Kernel Fisher Discriminant Analysis Using Leave-One-Out Cross Validation', *Neural Computation*, vol. 18, issue 4, pp 961 – 968

Bonga, M.W. 2005, 'An Overview of the South-African Iron, Manganese and Steel Industry During the Period 1984 – 2003', Report R45/2005, Directorate: Mineral Economics, Department of Minerals and Energy, South Africa

Curr, T.R., Nicol, K.C., Mooney, J.F. 1985, 'The 3.2 MVA Plasma Facility at Mintek', Council of Mineral Technology, South Africa, Retrieved: September 24, 2007, from http://www.pyrometallurgy.co.za/Mintek

Drouet, M.G., Nadeau, F. 1982, 'Acoustic measurement of the arc voltage applicable to arc welding and arc furnaces', *Journal of Physics E: Scientific Instrumentation*, vol. 15, issue 3, pp 265-269

Duda, R., Hart, P., Stork, D., 2001, 'Pattern Classification', 2nd ed., *John Wiley & Sons, Inc.*, United States of America

Edström, J. 0., Fauchais, P., V.R. Heberlein, J., Mac Rae, D. R., PhilBrook, W. O., Skogberg, J. (ed), 1987, *Plasma Technology in Metallurgical Processing*, 1st ed., Iron and Steel Society, United States of America

Evers, H. 1999, 'Arc Deflection in DC Smelters: Calculation, Design and Commissioning of Furnaces with Minimized Arc Deflection', Heavy Minerals Conference 1999, South Africa

Fisher, R. A., 1936, 'The Use of Multiple Measurements in Taxonomic Problems', *Annual of Eugenics*, vol. 7, pp. 179-188

Fukunaga, K., 1990, 'Introduction to Statistical Pattern Recognition', 2nd ed., *Academic Press*, United States of America, Orlando, FL.

Gous, M., 2006, 'An overview of the Namakwa Sands Ilmenite Smelting Operations', Southern African Pyrometallurgy, South African Institute of Mining and Metallurgy, pp 189-201

Haus, H. A., Melcher, J. R. 1989, 'Electromagnetic Fields and Energy', Prentice-Hall Inc, United States of America

Hsu, C., Chang, C., Lin, C., 2007, 'A Practical Guide to Support Vector Classification', Department of Computer Science National Taiwan, Retrieved: Sep 24, 2007, from http://www.csie.ntu.edu.tw/~cjlin

Jones, R.T., Reynolds, Q.C., Alpont, M.J. 2002, 'DC arc photography and modelling', *Minerals and Engineering*, vol. 15, no. 11, pp. 985-991

Jones, R.T., 2006, 'Southern African Pyrometallurgy 2006', South African Institute of Mining and Metallurgy, Johannesburg

Kang, H.J., Na, S.J. 2002, 'A Study on the Modeling of Magnetic Arc Deflection and Dynamic Analysis of Arc Sensor', *Welding Journal*, vol. 81, no. 1, pp 8-13

Knight, R., Murawa, M.J., Girgis, N.M., Reid, K.J., 1990, 'The Arc characteristics in Small Scale DC Plasma Arc Furnaces', *Plasma chemistry and plasma processing*, vol. 10, no. 2, pp 359-373

Kunze, J, Degel, R, 2004, 'Innovative Submerged Arc Furnace Technology for Non-Ferrous Metal Industries', *World of Metallurgy – ERZMETALL*, vol. 57, no. 3, pp 129-151

Kweyama, N. 2005, 'South African Ferrous Minerals Production Trends 1994-2003', Report R48/2005, Directorate: Mineral Economics, Department of Minerals and Energy, South Africa, 2005

Ladoux, P., Gianluca, P., Foch, H., Nuns, J. 2005, 'A Comparative study of AC/DC Conversters for High-Power DC Arc Furnace', *IEEE Transactions on Industrial Electronics*, vol. 52, no. 3, pp 747-757

Lanckriet, G.R.G., Christianini, N., Barlet, P., El Ghaoui, L., Jordan, M. I. 2004, 'Learning the Kernel Matrix with Semidefinite Programming', *Journal of Machine Learning*, vol 5, pp 27-72

Ma, T., Sarvinis, J., Voermann, N., Wasmund, B. 1996, 'Recent Developments in dc Furnace Design', *Challenges in Process Intensification Symposium*, Montreal Quebec, Canada, 1996

Marques de Sá, J.P, 2001, 'Pattern Recognition. Concepts, Methods and Applications', *Springer*, Germany

Maske, K.U., Reid, K.J. 1985, 'Metallurgical Reaction Philosophies of Transferred Arc Plasma Furnaces ', *Council of Mineral Technology*, South Africa, Retrieved: September 24 2007, from http://www.pyrometallurgy.co.za/Mintek

McRae, L.B., Barcza, N.A., Curr, T.R. 1985, 'The Application of Transferred-Arc Plasma to the Melting of Metal Fines', *Proceedings of the International conference on Mineral Science and Technology*, Haugton L.F. (ed), Randburg, Council of Mineral Technology, 1985, vol.2, pp 827-836

Mika, S. 2002, 'Kernel Fisher Discriminants'. PhD thesis, University of Technology, Berlin, October 2002

Mohan, N., Undeland, T.M., Undelan, W.P. 2003, 'Power Electronics Converters, Application and Design', 3rd ed., *John Wiley & Sons*, United States of America

Muller, H.G., Further, H., 1994, 'The VAI Electric Arc Furnace – a Proven Technology for Economical Steel Production', *SEAISI Quarterly*, vol. 24, nr. 4, pp 30-36

Proakis, J.G., Manolakis, D.G. 1995, 'Digital Signal Processing: Principles, Algorithms, and Application', 3rd ed., *Prentice Hall, Inc.,* United States of America

Russell, S., Norvig, P. 1995, 'Artificial Intelligence: A Modern Approach', 1st ed., *Prentice Hall, Inc.*, Upper Saddle River, New Jersey

Skowronski, M. D., Harris, J. G., 2003, 'Improving the Filter Bank of a Classical Speech Feature Extraction Algorithm', *IEEE Intl Symposium on Circuits and Systems*, Bangkok, Thailand, vol. 4, pp 281-284,

Stenkvist, S.-E., Bowman, B. 1987, 'The Properties and Practical Applications of High-Power Graphite-cathode d.c. Arc Plasma', *Plasma Technology in Metallurgical Processing*, The Iron and Steel Society, AIME, Chapter 8B, pp. 103-109

Takens, F. 1981, 'Detecting strange attractors in turbulence', *Dynamical Systems and Turbulence*, vol. 898, pages 366–381

Theodoris, S., Koutroumbas, K. 2004, 'Pattern Recognition', 2nd ed., *Academic Press*, United States of America

Tsai, N.S., Eagar, T.W. 1985, 'Distribution of the Heat and Current Fluxes in Gas and Tungsten Arcs', *Metallurgical Transactions B (Process Metallurgy)*, vol. 16B, no. 4, pp. 841-846

Zweben, S., Karasik, M. 2002, 'Laboratory experiments on arc deflection and instability', *U.S. Department of Energy: Office of Scientific and Technical information*, Retrieved: September 24, 2007, from http://www.osti.gov/bridge/

Appendix A

Printed Circuit Board (PCB) Design

A.1.Schematic Layout

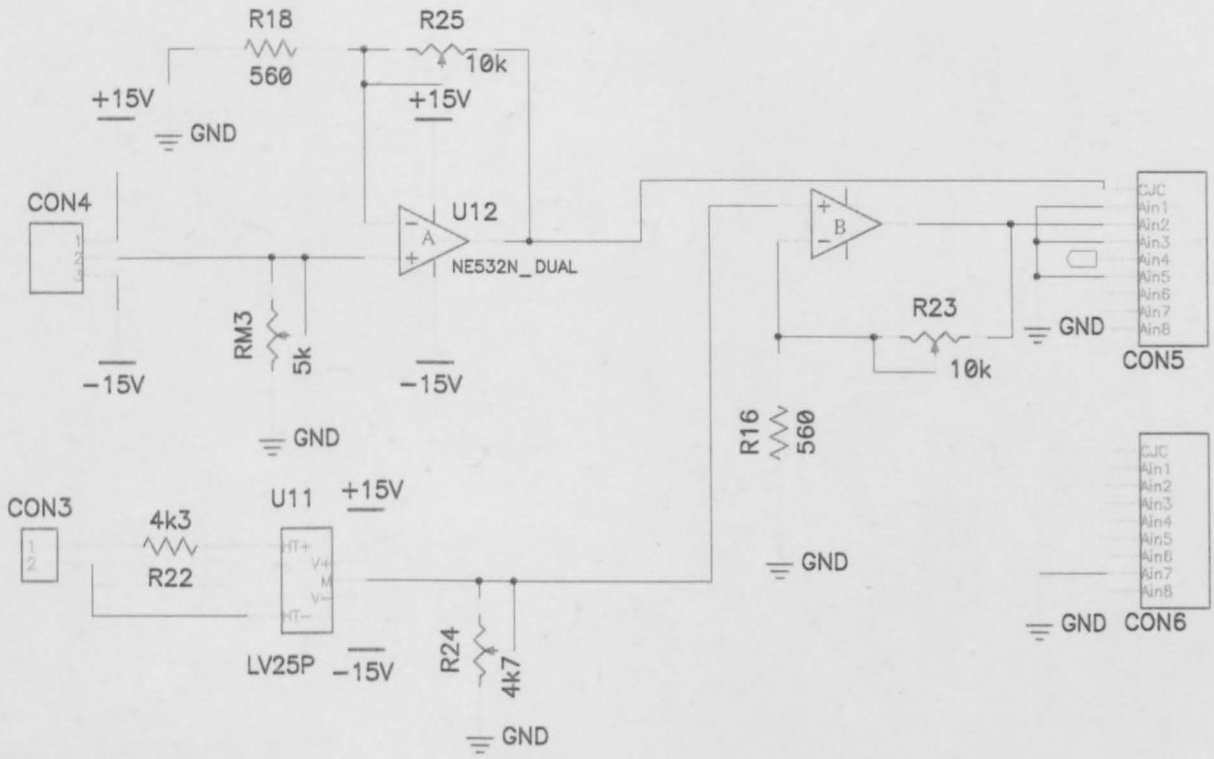

Figure A. 1. The schematic for the current and voltage signal amplifiers

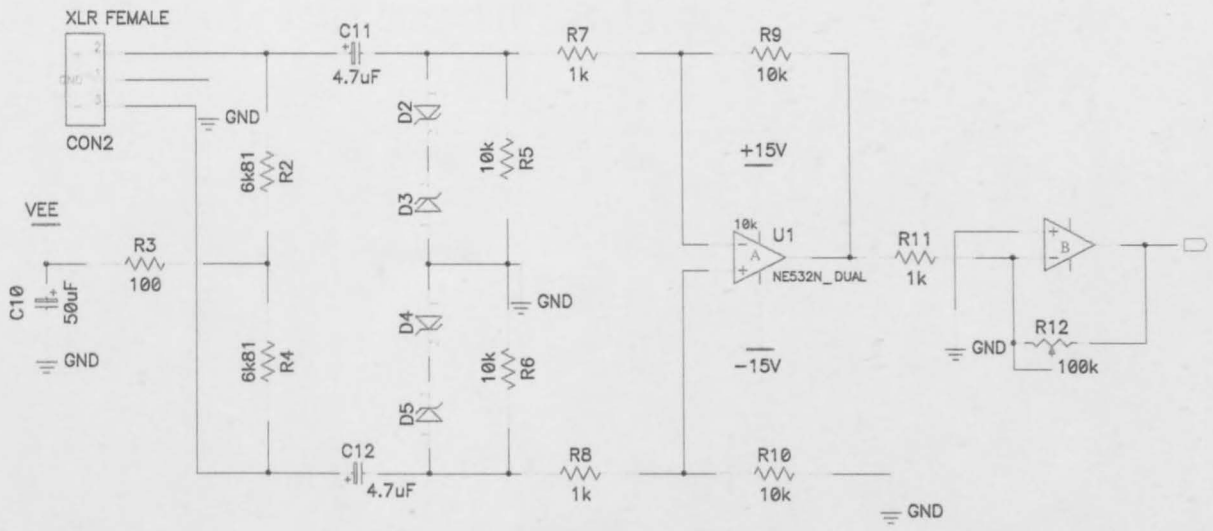

Figure A. 2. The preamplifier schematic.

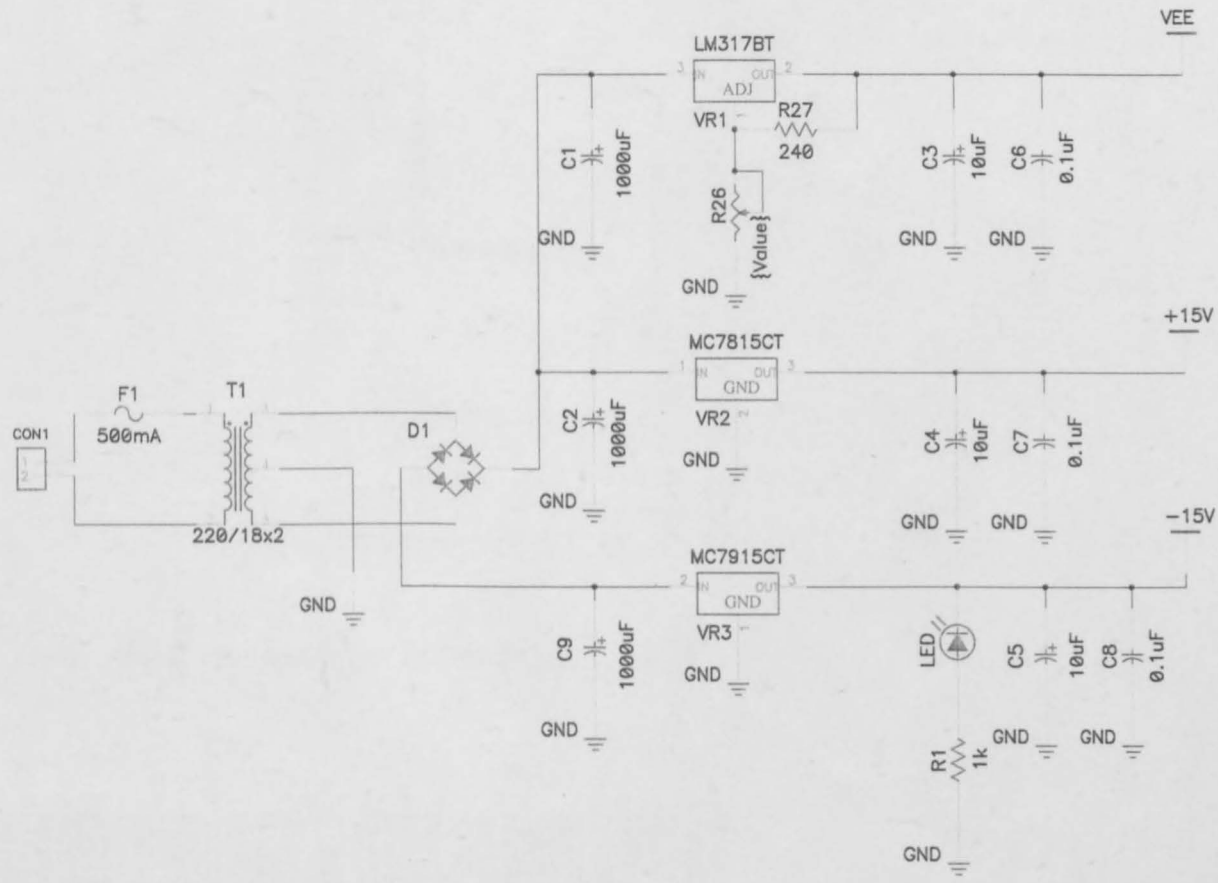

Figure A. 3. The power source schematic.

A .2. Printed circuit board (PCB) layout

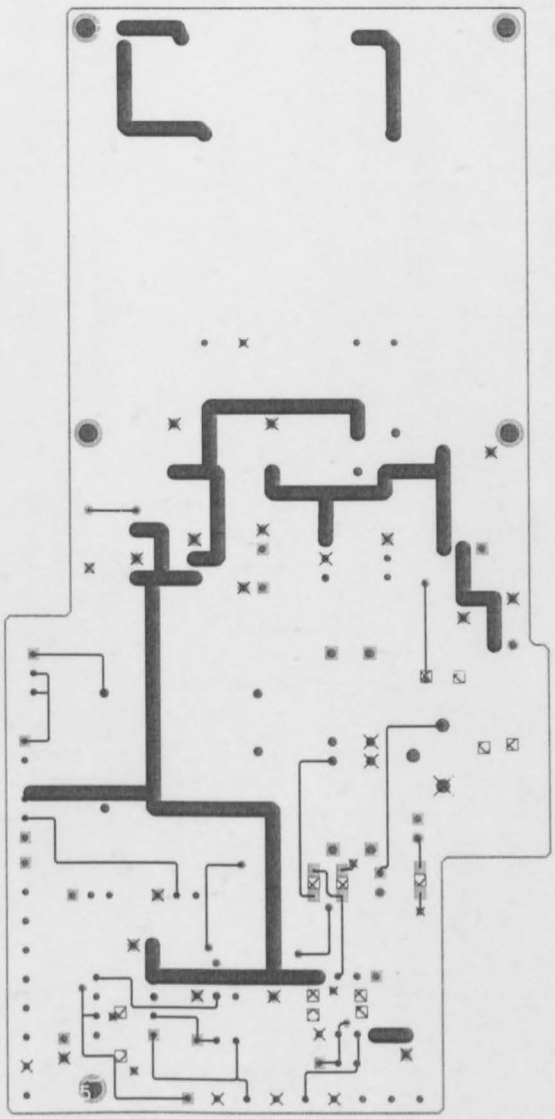

Figure A. 4. The top layer of the PCB.

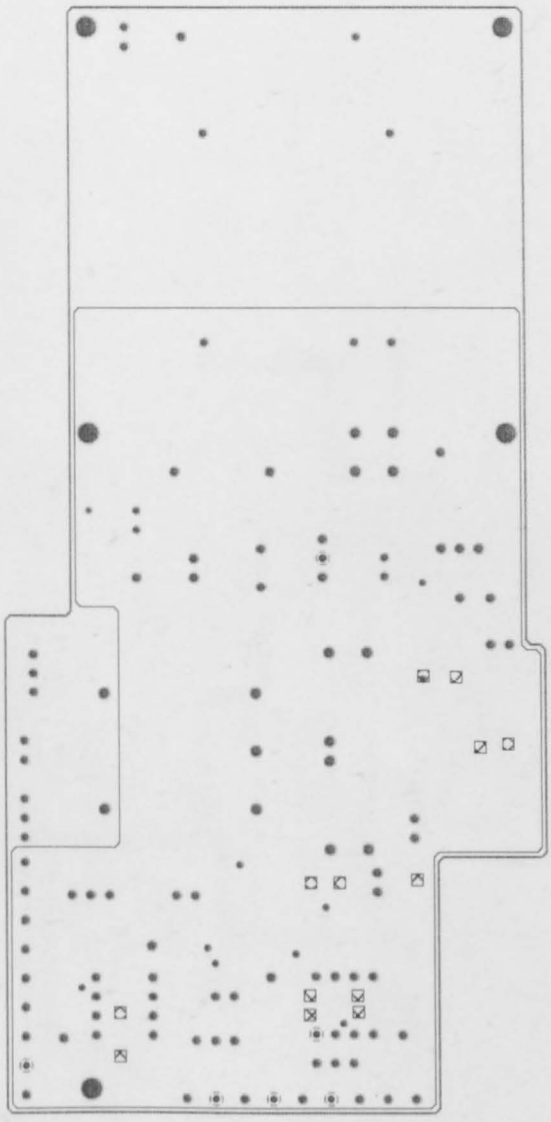

Figure A. 5. The middle layer of the PCB.

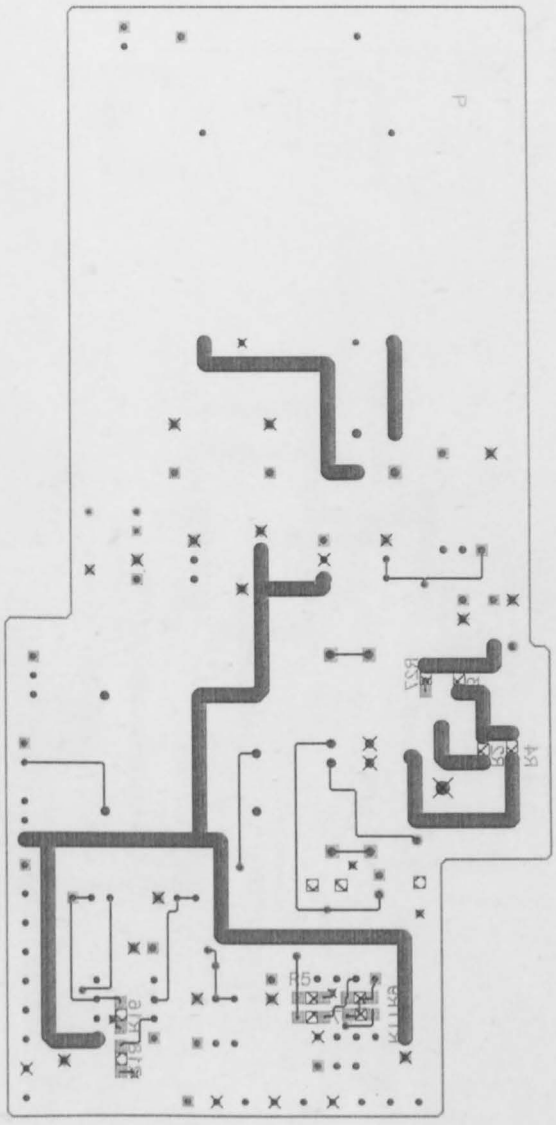

Figure A. 6. The bottom layer of the PCB.

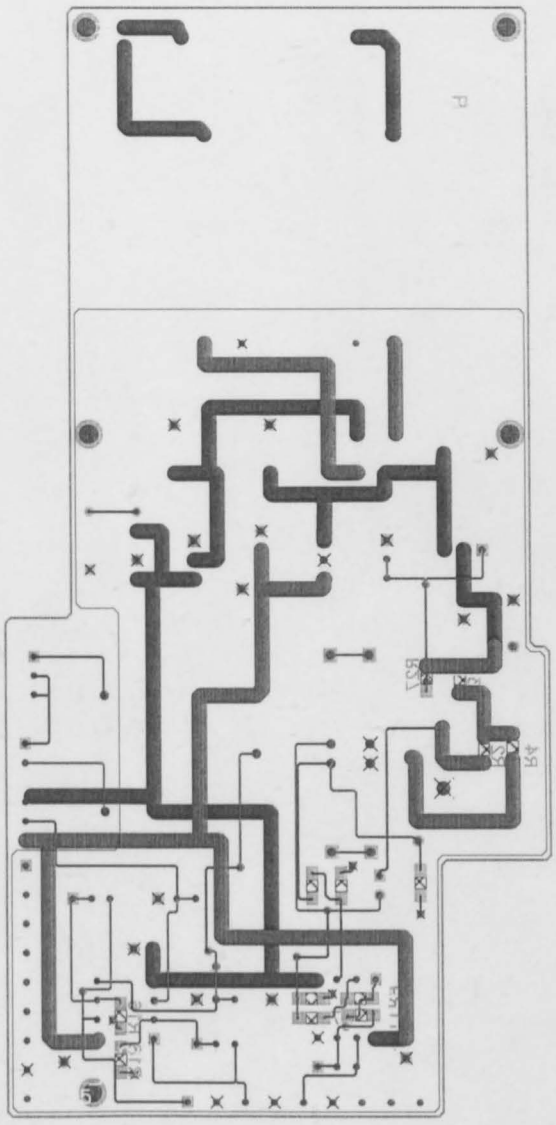

Figure A. 7. The complete PCB layout.